Computational investigation of the structural and electrolyte properties of the extended family of lithium (thio)boracite materials: $Li_4B_7O_{12}Cl$ and beyond

D. Cory Lynch,[1,*] Yan Li,[2,*] Pieremanuele Canepa,[2,3,4] and N. A. W. Holzwarth[5]

[1]*Department of Physics, Wake Forest University, Winston-Salem, North Carolina 27109, USA*
[2]*Department of Materials Science and Engineering, National University of Singapore, Singapore 119077, Singapore*
[3]*Department of Electrical and Computer Engineering, University of Houston, Houston, Texas 77204, USA*
[4]*Texas Center for Superconductivity at the University of Houston (TcSUH), Houston, Texas 77204, USA*
[5]*Department of Physics, Wake Forest University, Winston-Salem, North Carolina 27109, USA*

(Received 13 December 2023; revised 5 March 2024; accepted 15 May 2024; published 3 June 2024)

Motivated by previous investigations that showed very promising high ionic conductivities within relatively stable framework structures, we report a systematic first-principles study of the extended family of lithium (thio)boracites, consisting of eight chemical compositions. Three of the compositions—$Li_4B_7O_{12}Cl$, $Li_4Al_3B_4O_{12}Cl$, and $Li_6B_7S_{13}Cl$—are comparable to synthesized and analyzed materials reported in the experimental literature. The five additional compositions—$Li_4B_7S_{12}Cl$, $Li_4Al_3B_4S_{12}Cl$, $Li_6B_7O_{13}Cl$, $Li_6Al_3B_4O_{13}Cl$, and $Li_6Al_3B_4S_{13}Cl$—are predicted from the computational modeling and analysis presented in this paper. For each material, idealized ordered rhombohedral, cubic, or monoclinic ground-state structures are determined. Through various methodologies including thermodynamic, voltage window, and harmonic phonon analyses, stability is assessed for all eight Li (thio)boracite-derived compositions. Based on the dominant energetics of density functional theory, an analysis of the thermodynamically accessible phases predicts stability for $Li_4B_7O_{12}Cl$ only. The analysis of the voltage windows of these materials suggests that the sulfur materials are much more reactive in contact with lithium metal than their oxygen counterparts. This reactivity problem has been identified in other highly conducting solid electrolytes and various mitigation methods discussed in the literature look promising. Within the harmonic approximation, phonon analysis predicts that all eight materials are dynamically stable in their ground-state structures. Future investigations will focus on the performance of the family of lithium (thio)boracites, including ionic conductivity predictions and ion migration mechanisms.

DOI: 10.1103/PhysRevMaterials.8.065401

I. INTRODUCTION

Recently, there has been considerable interest in lithium boracite materials as fast ion conductors with possible application to all-solid-state battery technology. These materials are characterized by high-symmetry frameworks with void channels available for ion conduction. For the Li_4 boracites, a prototypical material was studied in the 1970s [1] with the composition $Li_4B_7O_{12}Cl$. More recently, Tan and coworkers [2] developed an efficient synthesis method and improved the room-temperature ionic conductivity of this material by two orders of magnitude over the conductivity reported by Jeitschko and coworkers [1]. Our group [3] computationally examined the structural properties and ion migration mechanisms of $Li_4B_7O_{12}Cl$. A related Li_4 boracite has been synthesized with aluminum substitutions on some of the boron sites by Kajihara and coworkers [4] and by Katsumata and coworkers [5] to form $Li_4Al_3B_4O_{12}Cl$, and has been found to have favorable ion conducting properties. In addition to the family of Li_4 boracite materials, evidence for an even more highly conducting "stuffed Li" thioboracite (Li_6) family of materials has appeared with the report in 2021 by Kaup and coworkers [6] of the synthesis and characterization of $Li_6B_7S_{13}I$.

Here we report the results of a detailed computational study of four combinations of components, considering both Li_4 and Li_6 stoichiometries, focusing on eight members of the Li (thio)boracite-derived family. Structural optimizations were performed, assuming ordered structures related to or derived from experimentally analyzed space groups. In addition to the three experimentally identified compounds—$Li_4B_7O_{12}Cl$, $Li_4Al_3B_4O_{12}Cl$, and $Li_6B_7S_{13}Cl$, five additional stoichiometries—$Li_6B_7O_{13}Cl$, $Li_6Al_3B_4O_{13}Cl$, $Li_4B_7S_{12}Cl$, $Li_6B_7S_{13}Cl$, and $Li_6Al_3B_4S_{13}Cl$—are predicted from simulations. The optimized structures and their phonon spectra are examined, as well as their synthesizability in terms of a convex hull construction and of the estimation of the electrochemical voltage windows.

The paper is organized as follows. Section II outlines the main computational methods used in this paper. Section III presents the idealized structural forms found by static lattice optimizations including four main optimized ordered structures as well as some additional optimized ordered structures having energies above that of the global minimum. Section IV examines the phase diagram of the Li (thio)boracite family in terms of a convex hull analysis while Sec. V extends the analysis of the static lattice formation energy results to infer the stability of these materials in battery conditions in terms of

*These authors contributed equally to this work.

estimation of voltage windows. Section VI presents the results of harmonic phonon analysis of the optimized structures of the eight electrolyte candidates. A summary and conclusions are presented in Sec. VII.

II. CALCULATIONAL METHODS

All calculations were performed using the Wake Forest University High Performance Computing Facility [7]. The computational methods were based on density functional theory (DFT) [8,9] and density functional perturbation theory (DFPT) [10–14], using the projector augmented wave (PAW) [15] formalism. The modified generalized gradient formulation known as PBEsol [16] was used to treat the exchange and correlation effects. The PAW basis and projector functions for Li, B, O, Al, S, and Cl were generated by the ATOMPAW code [17]. Simulations for idealized models of the studied crystals, usually in their primitive unit cells, were carried out using the ABINIT [18,19] and the QUANTUM ESPRESSO packages [20,21]. For a given stoichiometry of N_i atoms of each element i, results from optimizing the lattice structure of ordered arrangements of lithium ions within the (thio)boracite-derived frameworks provide structurally optimized DFT total electronic energies. As in our previous computational study on solid electrolytes [22], thanks to the Born-Oppenheimer approximation [23] where the atomic coordinates are treated as "static" classical point particles, and to the electronically insulating nature of these materials, it is reasonable to identify the optimized DFT total electronic energy as a good approximation to the static lattice internal energy $U_{SL}(\{N_i\})$. Well-converged plane-wave expansions—$|\mathbf{k}+\mathbf{G}|^2 \leqslant 70\,\text{Bohr}^{-2}$ and $|\mathbf{k}+\mathbf{G}|^2 \leqslant 81\,\text{Bohr}^{-2}$—were used with ABINIT and QUANTUM ESPRESSO, respectively. For approximating integrals over the Brillouin zone, uniform midpoint sampling was used with sampling volumes less than 10^{-3} (radians/Bohr)^3. Structural optimizations were carried out by using the conjugate gradient based algorithms implemented in the two codes, with residual forces magnitudes limited to less than 10^{-4} Ryd/Bohr. In this way, we find total energy differences between the two codes to be less than 0.002 eV/FU [eV/(formula unit) or 0.0001 eV/atom] for the materials in this study. In Secs. III, IV, and V, we focus on the static lattice internal energies $U_{SL}(N_i)$ of the materials, approximating the Helmholtz free energy as

$$F(T, V, \{N_i\}) \approx U_{SL}(\{N_i\}), \tag{1}$$

where T and V denote temperature and volume, respectively. Similar approaches have been found to be useful for the development of large materials databases such as the Materials Project [24] and the Open Quantum Materials Database [25,26]. Generally, lattice vibrations within the harmonic approximation, considered in Sec. VI, and other temperature-dependent effects, while important, are estimated to have energetic contributions of 0.05 eV/FU or less.

The present paper also benefited from the use of several public domain analysis tools such as FINDSYM [27] for identifying the space group structure of optimization outputs, VESTA [28] for structural visualization, and XMGRACE [29] for plotting.

III. IDEALIZED STRUCTURES

Two important components of the structural forms of the lithium (thio)boracite family of materials are the (thio)borate framework and the void regions containing the mobile Li ions and Cl or other halide counter ions. The framework structure is negatively charged, carrying a formal charge of -3 ($[B_7O_{12}]^{3-}$ for example) or -5 ($[B_7O_{13}]^{5-}$ for example) for the Li_4 or Li_6 materials, respectively. It is flexible enough to accommodate interconnected, corner-sharing anions including tetrahedral BO_4, AlO_4, BS_4, or AlS_4 units and, in some cases, planar triangular BO_3 or BS_3 units. Typically the halide ions occupy well-defined positions in the voids while the Li ions occupy various other sites in the void regions.

The experimental literature on Li (thio)boracite materials identifies their structures with the face-centered cubic $F\bar{4}3c$ (No. 219) [30] space group. This includes both the Li_4 and Li_6 materials [1,2,4–6,31–35], characterized with fractional occupancy on the Li sites. The beauty of these structures is that the $F\bar{4}3c$ space group allows for natural interstitial sites available for Li ion migration, which is consistent with the fractional occupancy deduced from diffraction analysis. In our previous study [3] of $Li_4B_7O_{12}Cl$, static lattice optimization results identified the existence of a fully ordered and more stable structure of face-centered $R3c$ (No. 161). Interestingly, from the viewpoint of group theory analysis, the rhombohedral structure could be predicted by noting that the $R3c$ space group is a simple subgroup of $F\bar{4}3c$. For the extended family of Li (thio)boracites, in addition to the $R3c$ structure, two other ordered structural forms, characterized by the $F\bar{4}3c$ and Cc space groups have been found to characterize the optimized ground-state structures for one or more of the eight members.

In order to present an overview of the results, the optimized lattice and other structural parameters in their conventional cell settings [30] together with the static lattice total energy differences from the density functional calculations are listed in Table I. While a systematic study of phase stability is presented in Sec. IV, here we focus on the comparisons within each of the four combinations of components, including both Li_4 and Li_6 stoichiometries. For this purpose, for each family of compositions, it is convenient to define the static lattice energy difference based on the $R3c$ structure of the Li_4 compound chosen as the reference. For family members having the Li_4 stoichiometries, $\Delta U_{SL}(\text{Li}_4\text{boracite})$ is defined as

$$\begin{aligned}\Delta U_{SL}(\text{Li}_4\text{boracite}) \equiv\ & U_{SL}(\text{Li}_4\text{boracite}) \\ & -U_{SL}(\text{Li}_4\text{boracite}[R3c]).\end{aligned} \tag{2}$$

For family members having the Li_6 stoichiometries, $\Delta U_{SL}(\text{Li}_6\text{boracite})$ is defined as

$$\begin{aligned}\Delta U_{SL}(\text{Li}_6\text{boracite}) \equiv\ & U_{SL}(\text{Li}_6\text{boracite}) \\ & -U_{SL}(\text{Li}_4\text{boracite}[R3c]) - U_{SL}(\text{Li}_2\text{X}).\end{aligned} \tag{3}$$

Here Li_2X represents the static lattice energy of one formula unit of $Fm\bar{3}m$ Li_2O or of $Fm\bar{3}m$ Li_2S as appropriate. These energies are listed in Table I in the column labeled ΔU_{SL} in units of eV/FU.

Here we see that for the $R3c$ structures, the conventional cell rhombohedral angle deviates from 90 degrees by less

TABLE I. Summary of the structural parameters and relative energies for the dominant structural forms of the (thio)boracites considered in this study. Here the column "SG" gives the space group based on the conventional cells listed in the crystallography tables [30]. The column "Lattice" lists the conventional cell lattice parameters in Angström units and "Angles" lists the lattice angles in degrees with the measured values in parentheses when available from the literature. The conventional cells for the $F\bar{4}3c$ and $R3c$ structures contain eight formula units while the conventional cells for the Cc structures contain four formula units. For all three structures, the primitive cells all contain two formula units; the Cartesian coordinates of the primitive lattices and the corresponding fractional atomic coordinates are all given in the Part I of the SM [36]. The column Tri/Tet parameterizes the (thio)borate framework anions in terms of the numbers of interconnected "triangular planar" vs "tetrahedral", (BO_3 or BS_3) vs (BO_4, BS_4 AlO_4, or AlS_4) framework components in a primitive cell. The column "Vol" lists the volume per formula unit in Angström^3 units. The column ΔU_{SL} lists the static lattice energy difference in eV/FU for each family of materials as described by Eqs. (2) and (3).

Formula	SG	Lattice	Angle	Tri/Tet	Vol	ΔU_{SL}
$Li_4B_7O_{12}Cl$	$R3c$	$a = 12.1$ (12.1410)[a]	$\alpha = 90.1$ (90.0)[a]	4/3	223.0	0.00
$Li_4B_7O_{12}Cl$	$F\bar{4}3c$	$a = 12.2$	$\alpha = 90.0$	4/3	224.8	0.21
$Li_6B_7O_{13}Cl$	$R3c$	$a = 12.2$	$\alpha = 89.4$	1/6	224.3	–1.58
$Li_6B_7O_{13}Cl$	Cc	$a = 15.0$	$\alpha = 90.0$	1/6	225.8	–1.26
		$b = 8.6$	$\beta = 124.7$			
		$c = 8.6$	$\gamma = 90.0$			
$Li_4Al_3B_4O_{12}Cl$	$R3c$	$a = 13.0$ (12.9687)[b]	$\alpha = 91.1$ (90.0)[b]	4/3	275.6	0.00
$Li_4Al_3B_4O_{12}Cl$	$F\bar{4}3c$	$a = 13.0$	$\alpha = 90.0$	4/3	272.0	1.19
$Li_6Al_3B_4O_{13}Cl$	$R3c$	$a = 13.0$	$\alpha = 88.3$	1/6	275.0	–0.22
$Li_6Al_3B_4O_{13}Cl$	Cc	$a = 16.0$	$\alpha = 90.0$	1/6	273.8	–0.40
		$b = 8.9$	$\beta = 127.1$			
		$c = 9.7$	$\gamma = 90.0$			
$Li_4B_7S_{12}Cl$	$R3c$	$a = 14.9$	$\alpha = 89.8$	4/3	415.7	0.00
$Li_4B_7S_{12}Cl$	$F\bar{4}3c$	$a = 14.9$	$\alpha = 90.0$	4/3	414.6	–0.05
$Li_6B_7S_{13}Cl$	$R3c$	$a = 15.1$ (15.245)[c]	$\alpha = 89.2$ (90.0)[c]	0/7	431.3	–0.96
$Li_6B_7S_{13}Cl$	Cc	$a = 18.5$	$\alpha = 90.0$	0/7	429.9	–1.05
		$b = 10.5$	$\beta = 124.6$			
		$c = 10.8$	$\gamma = 90.0$			
$Li_4Al_3B_4S_{12}Cl$	$R3c$	$a = 16.1$	$\alpha = 89.6$	4/3	516.9	0.00
$Li_4Al_3B_4S_{12}Cl$	$F\bar{4}3c$	$a = 15.8$	$\alpha = 90.0$	4/3	489.0	0.85
$Li_6Al_3B_4S_{13}Cl$	$R3c$	$a = 16.1$	$\alpha = 87.8$	0/7	519.7	–0.34
$Li_6Al_3B_4S_{13}Cl$	Cc	$a = 19.8$	$\alpha = 90.0$	0/7	508.2	–0.65
		$b = 10.8$	$\beta = 126.1$			
		$c = 11.8$	$\gamma = 90.0$			

[a]Reference [1] for $Li_4B_7O_{12}Cl$ in the $F\bar{4}3c$ structure (with fractional occupancy). Similar results are reported in Ref. [5].
[b]Reference [5] for $Li_4Al_3B_4O_{12}Cl$ in the $F\bar{4}3c$ structure (with fractional occupancy).
[c]Reference [6] for $Li_6B_7S_{13}I$ in the $F\bar{4}3c$ structure (with fractional occupancy).

than 3 degrees, indicating that the rhombohedral distortions relative to cubic are small. For the three materials that can be compared with the experimental literature, the corresponding fractional coordinates are listed in Appendix A while the full structural parameters of the primitive cells are given in the Part I of the Supplemental Material (SM) [36]. In order to widen the scope of structural features, Table I also parameterizes the (thio)borate framework in terms of the numbers of interconnected "triangular planar" (BO_3 or BS_3) versus "tetrahedral" (BO_4, BS_4, AlO_4, or AlS_4) framework components in a primitive cell in the column labeled "Tri/Tet" and also the volume per formula unit in units of Å^3 in the column labeled "Vol".

Details for the $R3c$, $F\bar{4}3c$, and Cc structural forms are presented in Secs. III A, III B, and III C, respectively. A summary of additional structural analyses is presented in Sec. III D.

A. Structures characterized by the *R3c* space group

There are many equivalent rhombohedral lattice conventions in the literature. In this paper, we follow the convention described in Ref. [3] since it most easily reveals the structural relationship with the related face-centered-cubic structure. In performing the static lattice structural analysis of the eight members of our Li (thio)boracite family, we find optimized ordered $R3c$ structures for all of them. For the Li_4 (thio)boracites, the rhombohedral distortion (Ref. [3]) follows from the low-temperature single crystal analysis of $Li_4B_7O_{12}Cl$ results of Jeitschko *et al.* [1]. The conventional cell of this crystal has 32 Li sites. At low temperatures, 24 Li sites with Wyckoff label 24*c* are fully occupied while 25% of the sites with Wyckoff label 32*e* are occupied. This partial occupancy causes the rhombohedral distortion to the $R3c$ space group, which is a subgroup of the $F\bar{4}3c$ space group. In this case, the conventional face-centered $R3c$ structure fully accommodates the eight Li sites with Wyckoff label 8*a*. The remaining 24 empty Li sites are designated by the Wyckoff label 24*b*, which are available as "natural interstitial" sites, participating in the Li ion mobility.

Table I shows that the structural parameters computed for $R3c$ $Li_4B_7O_{12}Cl$ are very close to experimental results

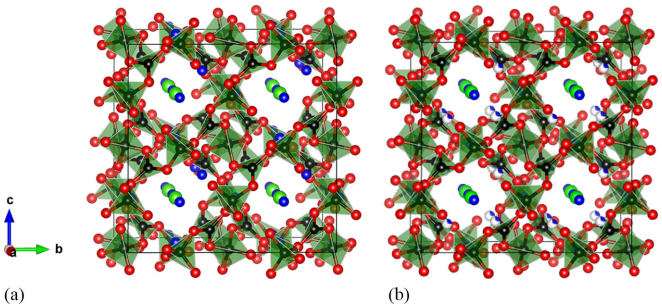

FIG. 1. Visualization of a conventional unit cell of $Li_4B_7O_{12}Cl$ in (a) its computed optimized structure and (b) the experimental structure of Ref. [1]. Li, B, O, and Cl are represented with blue, black, red, and light green balls; green shaded polyhedra indicate the BO_3 and BO_4 framework components. The fractionally occupied Li sites in the experimental structure are indicated with balls shaded 25% blue and 75% white.

deduced from the diffraction analysis of the $F\bar{4}3c$ structure [1]. The slight rhombohedral distortion, with the conventional cell rhombohedral angle of 90.1 degrees compared with ideal cubic angle of 90 degrees, is also evident in Fig. 1; the conventional cell fractional coordinates from the optimization are compared with the corresponding results from experiment in Appendix A, while the full structural parameters of the primitive cell for the optimized structure are given in Part I of the SM [36].

Similarly, Table I shows that the structural parameters computed for $R3c$ $Li_4Al_3B_4O_{12}Cl$ are very close to experimental results deduced from the diffraction analysis of the $F\bar{4}3c$ structure [4]. These results are visualized in Fig. 2; the conventional cell fractional coordinates from the optimization are compared with the corresponding results from experiment in Appendix A, while the full structural parameters of the primitive cell for the optimized structure are given in the Part I of the SM [36]. In this case, we see that the computed rhombohedral distortion is again small, with the conventional

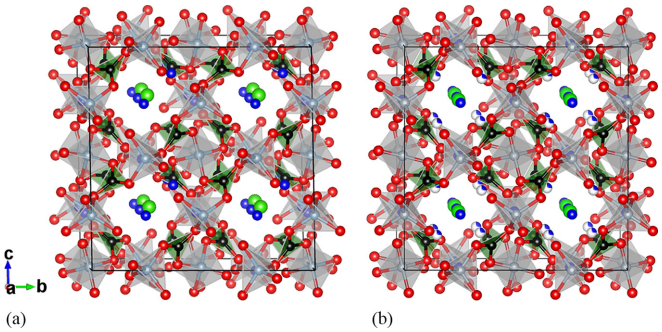

FIG. 2. Visualization of a conventional unit cell of $Li_4Al_3B_4O_{12}Cl$ in (a) its computed optimized structure and (b) the experimental structure of Ref. [4]. Li, Al, B, O, and Cl are represented with blue, grey, black, red, and light green balls; grey shaded tetrahedra indicate AlO_4 components and dark green shaded triangles indicate the BO_3 components of the framework. The fractionally occupied Li sites in the experimental structure are indicated with balls shaded 25% blue and 75% white.

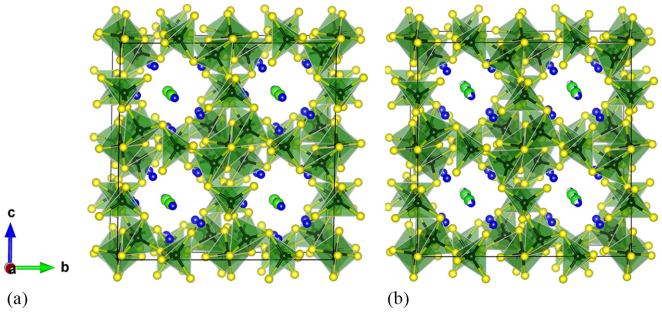

FIG. 3. Visualization of a conventional unit cell of $Li_6B_7S_{13}Cl$ in (a) its computed optimized $R3c$ structure and (b) the experimental structure of $Li_6B_7S_{13}I$ analyzed in Ref. [6]. Li, B, S, and Cl (or I) are represented with blue, grey, black, yellow, and light green balls; dark green shaded tetrahedra indicate BS_4 components of the framework. The fractionally occupied Li sites in the experimental structure are indicated with balls shaded 75% blue and 25% white.

cell rhombohedral angle of 91.1 degrees, compared with the ideal cubic angle of 90 degrees.

A similar group theory analysis can be applied to the Li_6 (thio)boracites. In this case, the $F\bar{4}3c$ conventional cell, if we assume that Li sites with Wyckoff label 24c are fully occupied, the remaining Li's would partially occupy the sites with Wyckoff labels 32e at the level of 75%. With the rhombohedral distortion, the conventional cell of the $R3c$ structure accommodates the Li sites with Wyckoff label 24b while the remaining eight empty Li sites are associated with the Wyckoff label 8a, which are available as "natural interstitial" sites, which facilitate Li ion mobility. These results are visualized in Fig. 3; the conventional cell fractional coordinates from the optimization are compared with the corresponding results from experiment in Appendix A, while the full structural parameters of the primitive cell for the optimized structure are given in the Part I of the SM [36]. In this case, the rhombohedral distortion is small, with rhombohedral angle of 89.2 degrees compared with 90 degrees for ideal cubic structure. The structure is visualized in Fig. 3 and the fractional coordinates are given in Table VI. As pointed out in Sec. VI, harmonic phonon analysis finds that this structure has some imaginary modes in a small volume of the Brillouin zone near $\mathbf{q} = 0$, indicating some dynamic instability. Further, as pointed out in Sec. III C, it is possible to find a lower-energy ordered structural form for $Li_6B_7S_{13}Cl$ than the $R3c$ structure. Interestingly, the experimental diffraction analysis of this structure by Kaup and coworkers [6] visualized in Fig. 3 finds a different fractional occupancy pattern for the $F\bar{4}3c$ cubic structure. They find that Li ions fully occupy the sites with Wyckoff labels 32e while partially occupying the sites with Wyckoff labels 24c at the level of 66.7%.

An interesting wrinkle to the structural analysis of $Li_6B_7S_{13}Cl$, is the possibility of a tetragonal phase, which Kaup and coworkers [6] identified in their experimental and modeling work. Our static lattice density functional analysis also found such a structure with $\Delta U_{SL} = -1.00$ eV/FU as defined in according to Eqs. (2) and (3). However, in the lattice vibrational analysis of this structure, we found imaginary phonon modes throughout the Brillouin zone for this structure, as did Kaup and coworkers [6]. Because of the dynamic

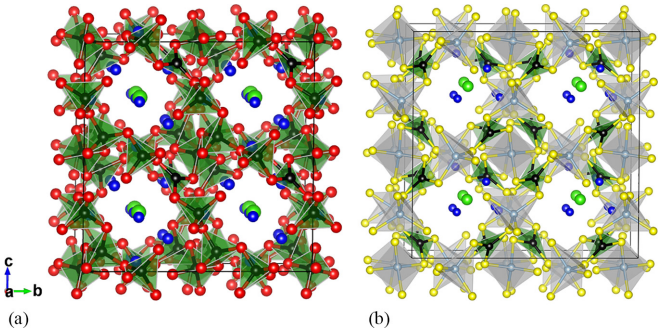

FIG. 4. Visualization of conventional unit cells of (a) $Li_6B_7O_{13}Cl$ and (b) $Li_4Al_3B_4S_{12}Cl$ in their computed optimized $R3c$ structures. Li, Al, B, O, S, and Cl are represented with blue, grey, black, red, yellow, and light green balls; dark green shaded polyhedra indicate BO_3/BS_3 and BO_4 components of the framework and the AlS_4 components are indicated with grey tetrahedra.

instability of this structure, it was not considered further in this paper.

Of the predicted but not yet experimentally realized members of the lithium boracite family, $Li_6B_7O_{13}Cl$ and $Li_4Al_3B_4S_{12}Cl$ are found to optimize in the $R3c$ structure. Their conventional unit cells are visualized in Fig. 4.

B. Structures characterized by the $F\bar{4}3c$ space group

The $F\bar{4}3c$ structure is another structural motif that logically follows from experimental evidence. The group theory analysis suggests that the Li_4 (thio)boracites can be ordered if the 32 Li ions fully occupy the sites with Wyckoff label 32e. As shown in Table I, this structure is energetically favored for $Li_4B_7S_{12}Cl$, but not for the other Li_4 family members. The $R3c$ and $F\bar{4}3c$ structures of $Li_4B_7S_{12}Cl$ are visualized in Fig. 5.

C. Structures characterized by the Cc space group

Another structural motif follows from the study of Kaup and coworkers [6] who also observed $Li_6B_7S_{13}I$ in a lower-symmetry structural form. Rather than the tetragonal structure

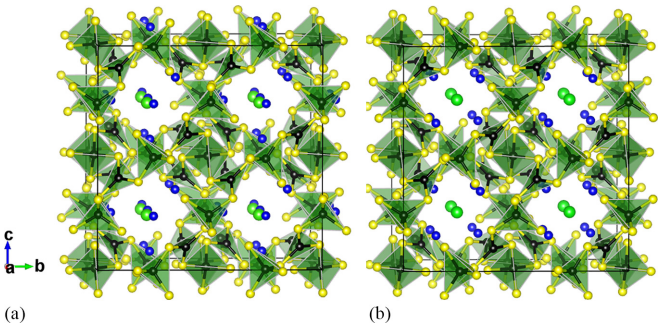

FIG. 5. Visualization of a conventional unit cell of $Li_4B_7S_{12}Cl$ in (a) its computed optimized structure with $R3c$ symmetry and (b) its computed optimized structure with $F\bar{4}3c$ symmetry, found to be energetically favorable. Li, B, S, and Cl are represented with blue, grey, black, yellow, and light green balls; dark green shaded tetrahedra indicate BS_4 components of the framework.

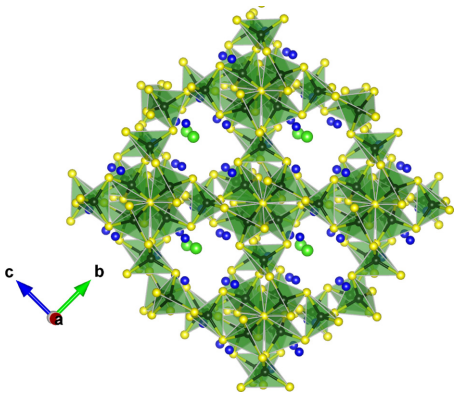

FIG. 6. Structure of $Li_6B_7S_{13}Cl$ in its computed optimized structure with Cc symmetry, visualized using multiples of the nearly orthorhombic cell defined in Eq. (5). Li, B, S, and Cl are represented with blue, grey, black, yellow, and light green balls; dark green shaded tetrahedra indicate BS_4 components of the framework.

suggested by simulations and experimental analysis of their study, we found a lower-energy centered monoclinic structure with the space group Cc (No. 9) [30]. The discovery of the Cc structure was initially made by performing structural optimization of configurations of $Li_6B_7S_{13}Cl$ generated during molecular dynamics simulations. The conventional cell of this base-centered monoclinic structure, consistent with Table I is given in cartesian coordinates by

$$\mathbf{a}_c = a\hat{\mathbf{x}} \quad \mathbf{b}_c = b\hat{\mathbf{y}} \quad \mathbf{c}_c = c(\cos\beta\hat{\mathbf{x}} + \sin\beta\hat{\mathbf{z}}). \tag{4}$$

For illustrating the similarities to the framework and void structures found in other (thio)boracites, a nearly orthorhombic supercell having the same volume and number of atoms (108) can be constructed with lattice parameters

$$\mathbf{a}_s = \mathbf{a}_c + \mathbf{c}_c, \quad \mathbf{b}_s = \mathbf{b}_c, \quad \mathbf{c}_s = \mathbf{c}_c. \tag{5}$$

This is shown in Fig. 6.

As indicated in Table I, we have found Cc structures for all of Li_6 (thio)boracites of this study. Interestingly, except for $Li_6B_7O_{13}Cl$, these Cc structures are computed to be their most stable structural forms. It is also interesting to note that the optimized structures for $Li_6B_7O_{13}Cl$ have a smaller volume per formula unit in the $R3c$ phase relative to the Cc phase, while $Li_6B_7S_{13}Cl$, $Li_6Al_3B_4O_{13}Cl$, and $Li_6Al_3B_4S_{13}Cl$ all have a smaller volume per formula unit in the Cc phase relative to the $R3c$ phase. To our knowledge, these Cc structures have not yet been observed for any of these materials. The predicted Cc structures of $Li_6Al_3B_4O_{13}Cl$ and $Li_6Al_3B_4S_{13}Cl$ are visualized in Fig. 7.

D. Search for additional structures

With a view toward extending the structural analysis of Li (thio)boracite family members, we conducted a few additional structural searches, focusing on the possibility of forming ordered stable structures with monoclinic (Cc) symmetry for the Li_4 (thio)boracites and on the possibility of forming order stable structures with cubic ($F\bar{4}3c$) symmetry for the Li_6 (thio)boracites.

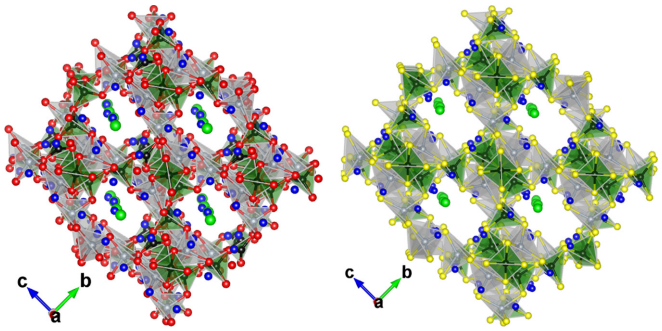

FIG. 7. Structures of $Li_6Al_3B_4O_{13}Cl$ (a) and $Li_6Al_3B_4S_{13}Cl$ (b) as computed optimized structure with Cc symmetry, visualized using multiples of the nearly orthorhombic cell defined in Eq. (5). Li, B, O, S, and Cl are represented with blue, grey, black, red, yellow, and light green balls; shaded planar triangles and tetrahedra indicate BO_3, BO_4, BS_4 (dark green), or AlS_4 (grey) components of the framework.

In the search for the Li_4 (thio)boracites with Cc symmetry, we examined each of the optimized Li_6 (thio)boracites in their Cc structure and systematically considered the distinct ways to remove one unit of Li_2O or Li_2S per formula unit while maintaining the Cc symmetry. It is convenient to work with primitive cells, which contain 2 formula units of the Li (thio)boracite and for which the Cc symmetry requires each distinct site to be paired with another symmetry related site. The distinct choices then involve finding 1 pair of symmetry related O or S atoms and two pairs of symmetry related Li atoms. By comparing the analysis of the experimental x-ray patterns based on the $F\bar{4}3c$ structure with fractional occupancy of the Li sites for $Li_4B_7O_{12}Cl$ [1] and for $Li_6B_7S_{13}Cl$ [6], the choice of the symmetry related O/S atoms to be removed could be reasonably associated with Wyckoff label a, missing in the Li_4 structure but occupied in the Li_6 structure. In addition to this fixed choice, the removed pair of O/S atoms (as adjusted to their equivalent locations in the Cc structure), two pairs of Li sites from among six distinct pairs had to be chosen for removal to make 15 distinct candidate configurations. For each of the Li_4 (thio)boracite compositions and each of their 15 candidate configurations, density functional optimizations were performed within the Cc symmetry constraint. The results find that lowest energy Li_4 (thio)boracite materials having the Cc structure have higher energy than their $R3c$ counterparts. For $Li_4B_7S_{12}Cl$, $U_{SL}^{Cc} - U_{SL}^{R3c} = +0.05$ eV/FU. Interestingly, as mentioned above, the ground-state structure of this composition has an ordered $F\bar{4}3c$ structure with $U_{SL}^{F\bar{4}3c} - U_{SL}^{R3c} = -0.05$ eV/FU. For the other three compositions, $U_{SL}^{Cc} - U_{SL}^{R3c}$ is considerably larger, ranging from 0.32 to 1.91 eV/FU.

In the search for the Li_6 (thio)boracites with ordered $F\bar{4}3c$ structures, we also performed density functional optimizations on a number of initial configurations, within the $F\bar{4}3c$ symmetry. Here, the (thio)boracite framework was initialized with a knowledge of corresponding experimental analysis of $Li_6B_7S_{13}I$ [6], while the ordered Li candidate configurations were chosen on sites with Wyckoff labels f or g, as is consistent with the $F\bar{4}3c$ space group. Since these sites only depend on one variable, we simply performed a coarse search of $x = \{0.1, 0.2, 0.3, 0.4\}$ and relaxed the structures to find the lowest energy, again ensuring it maintained the starting $F\bar{4}3c$ symmetry. The lowest-energy $F\bar{4}3c$ Li_6 structures found from this limited search were all structures with Li fully occupying the g sites and they all had much higher static lattice energies than their corresponding $R3c$ structures, ranging from 1.5 to 4.75 eV/FU higher energy. This ensures that these structures, even if metastable, will be more likely to be found in the lower energy $R3c$ or Cc structures.

These limited structural optimization studies provide further evidence that Table I includes the lowest-energy structures, including the ground-state static lattice structures, of Li (thio)boracite family of materials of this study.

More information about the electronic structures of the 16 Li (thio)boracite materials listed in Table I is given in Fig. 1, Sec. II of Part I of the SM [36] in the form of the valence band electronic partial density of states (PDOS). (Note that in this paragraph and in the corresponding section of Part I of the SM, "PDOS" refers to the electronic partial density of states.) From these plots, it is possible to make the following qualitative observations. It is clear that all of these materials are electronically insulating as expected. Interestingly, the PDOS plots are remarkably similar, particularly within each of the four compositions considered, for their four different optimized lattice structures. For all of the structures, the PDOS contributions from occupied states of Cl are highly peaked, consistent with their nonbonding attributes due to their location in the void regions of the structures. By contrast, PDOS contributions from occupied states involving the framework components B, Al, O, and S have much broader curves, consistent with their covalent bonding attributes. Apart from contributions from the localized Cl states, the top of the valence bands of these materials are dominated by O or S contributions, consistent with filled bound states associated with the atomic $2p$ or $3p$ levels. The PDOS contributions for Li in the occupied states have negligible magnitude, consistent their description as positive Li^+ ions in these materials.

IV. EQUILIBRIUM PHASE DIAGRAMS

In this section, we consider a more comprehensive analysis of the constituents of the Li (thio)boracite family of materials in order to reveal a holistic understanding of their phase equilibria. To accomplish this goal, we employ phase diagrams as a powerful analytical tool, as previously outlined by Ong *et al.* (2008) [37]. Ideally, the evaluation of phase stability for the solid materials of interest hinges upon the Helmholtz free energy $F(T, V, \{N_i\})$ as a function of temperature T, volume V, and numbers $\{N_i\}$ of constituents i.

As shown in Sec. VI, the energetic effect of lattice vibrations in the temperature range of $0\ \text{K} \leqslant T \leqslant 300\ \text{K}$ is estimated to be less than 0.05 eV/FU for the materials under investigation. Additionally, some of the materials of interest occur in gaseous form. The internal energy of an ideal gas approximates 0.03 eV/atom. For the few metallic materials in this study, the contributions to the temperature-dependent electronic heat capacity at 300 K is also negligibly small. These three contributions collectively constitute a minor fraction of the electronic binding energies, justifying the

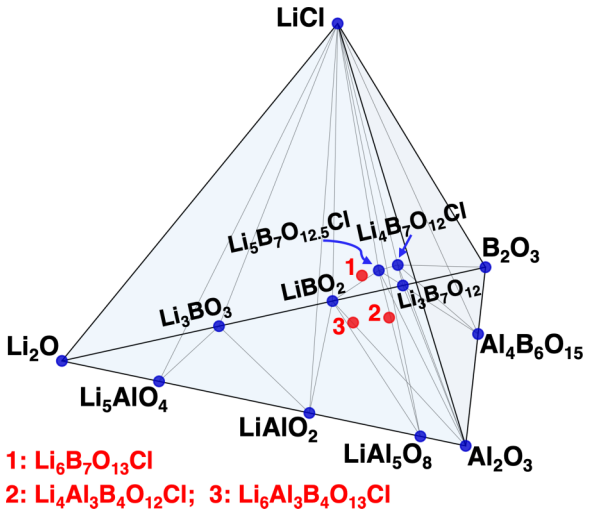

FIG. 8. Phase diagram of the quaternary subsystem of the Li-Al-B-O-Cl system, with stable phases represented by blue markers. While $Li_4B_7O_{12}Cl$ is calculated to be stable, the other three boracite materials, as listed at the bottom with numeric labels, are marked as unstable with red nodes on the diagram.

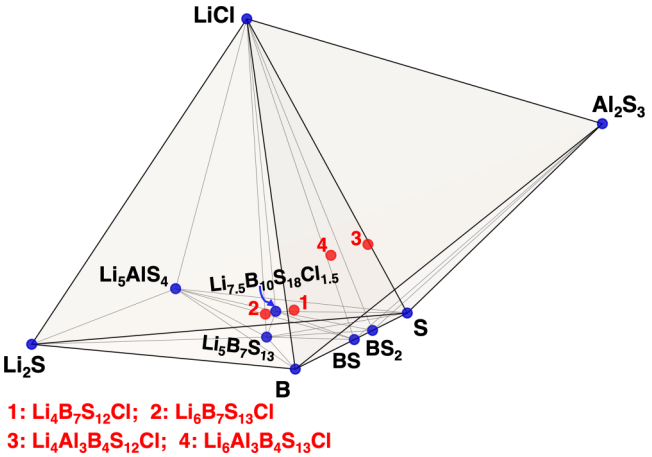

FIG. 9. Phase diagram of the pentagonal subsystem of the Li-Al-B-S-Cl system, with stable phases represented by blue markers. The four thioboracite materials, as listed at the bottom with numeric labels, are marked as unstable with red nodes on the diagram.

approximation of $F(T, V, \{N_i\})$ by its dominant electronic structure contribution given in Eq. (1). In this context, the focus is on $U_{SL}(\{N_i\})$, the static lattice energy determined from optimizing the static lattice density functional theory energy as described in Sec. II, using the QUANTUM ESPRESSO package [21] with the PBEsol [16] exchange-correlation functional.

In addition to the eight members of the Li (thio)boracite family, the elemental materials and compounds considered in this analysis were those within the composition spaces of Li-Al-B-O-Cl or Li-Al-B-S-Cl as listed in a comprehensive database—Inorganic Crystal Structure Database (ICSD) [38]. For each elemental and compound material, all the relevant initial structures were optimized to find the lowest value of $U_{SL}(\{N_i\})$. In some cases, such as for elemental O and Cl, the lowest value of $U_{SL}(\{N_i\})$ was found to correspond to a crystalline molecular crystal of dimer O_2 and Cl_2. Similar approaches have been used in the Materials Project [24] and the Open Quantum Materials Database [25,26]. The Python library Pymatgen (Python Materials Genomics) [39] was employed to construct the phase diagrams and we represent them in Figs. 8 and 9 for the boracite and thioboracite materials, respectively.

In order to quantify the energy calculations, it is convenient to introduce the concept of normalized formation energy based on the optimized static lattice energies $U_{SL}(\{N_i\})$. For example, considering the compound $LiAlB_{14}$ consisting of 16 atoms, which undergoes decomposition into its constituent elements in their standard forms,

$$LiAlB_{14} \rightarrow Li + Al + 14B, \tag{6}$$

the normalized formation energy is defined as

$$E_f(LiAlB_{14}) \equiv \frac{U_{SL}(LiAlB_{14}) - U_{SL}(Li) - U_{SL}(Al) - 14U_{SL}(B)}{16}. \tag{7}$$

All of the normalized formation energy results examined within this study are listed in Table VIII, which is available in Appendix B. This includes the complete list of materials, along with the space group of their lowest-energy structures, and the corresponding calculated normalized formation energies.

In the field of computational material science, the term "energy above the hull" $E_{\text{hull}}^{\text{above}}(\text{R})$, is commonly used to quantify the stability of compounds, distinguishing between stable and unstable phases depicted in phase diagrams [40]. This metric arises from the process of minimizing formation energies as computed by Eq. (7) within the composition space. It can be conceptualized as the energetic deviation from $E_f(\text{R})$ of compound R to the convex hull line. For a compound R that is stable and resides on the convex hull, the energy above the hull is quantified as zero,

$$E_{\text{hull}}^{\text{above}}(\text{R}) = 0. \tag{8}$$

In contrast, for an unstable compound R, the value of $E_f(\text{R})$ is greater than zero and measures the minimum reduction in formation energy for R to reach stability on the convex hull. If a stable counterpart R′ sharing the same stoichiometry as the unstable R resides on the hull, then $E_{\text{hull}}^{\text{above}}(\text{R})$ reflects the energy difference in their formation energies,

$$E_{\text{hull}}^{\text{above}}(\text{R}) = E_f(\text{R}) - E_f(\text{R}'). \tag{9}$$

In another scenario where the compound R is unstable and decomposes into a combination of stable products P_i, the energy above the hull is determined by the decomposition energy and approximated as

$$E_{\text{hull}}^{\text{above}}(\text{R}) = E_f(\text{R}) - \frac{1}{N_{\text{R}}} \sum_i x_i N_{\text{P}_i} E_f(\text{P}_i). \tag{10}$$

In this context, N_{R} and N_{P_i} denote the total number of atoms in R and the ith product P_i, respectively. The value of x_i specifies the stoichiometric coefficients for P_i in R such that $\sum_i x_i N_{\text{P}_i} = N_{\text{R}}$.

The tabulated values of $E_{\text{hull}}^{\text{above}}(\text{R})$ for compounds in the Li-Al-B-O-Cl or Li-Al-B-S-Cl composition spaces are

presented in Table VIII. The results for the eight compositions indicate that $Li_4B_7O_{12}Cl$ is the only material that is thermodynamically stable, with a hull energy of zero. Among the remaining compounds, both experimentally observed materials, $Li_4Al_3B_4O_{12}Cl$ [4,5] and $Li_6B_7S_{13}Cl$ [6], along with our predicted materials, namely $Li_6B_7O_{13}Cl$ and $Li_4B_7S_{12}Cl$, as well as the Al-doped boracite variants $Li_6Al_3B_4O_{13}Cl$, $Li_4Al_3B_4S_{12}Cl$, and $Li_6Al_3B_4S_{13}Cl$, were identified as unstable. Interestingly, for the unstable lithium boracites, both with and without aluminum substitution (entries #69–72 in Table VIII), a common decomposition product is $Li_5B_7O_{12.5}Cl$ (entry #66), which was experimentally identified in Refs. [34,41,42] and modeled in Ref. [3]. These unstable (thio)boracite materials exhibit values of $E_{\rm hull}^{\rm above}(\rm R)$ that range from 0.003 to 0.09 eV/atom, which are relatively modest. Such low values suggest that these materials could potentially achieve entropy-driven stabilization at high temperatures, analogous to the stabilization mechanisms observed in many metastable Li/Na ion conductors, where the metastability is predominantly attributed to the high intrinsic mobility of Li/Na ions within their structures. Additionally, kinetic factors, such as substantial energy barriers to phase transformations and decomposition reactions, can significantly influence the predominance of particular crystal structures. In some cases, materials with nonzero $E_{\rm hull}^{\rm above}(\rm R)$ values can be successfully synthesized by modulating the processing conditions to slow down phase transition rates, thus allowing synthesis to precede any potential decomposition. An exemplary case is provided by the experimentally synthesized $Li_4Al_3B_4O_{12}Cl$ [4], which exhibits an $E_{\rm hull}^{\rm above}(\rm R)$ value of 0.053 eV/atom.

The compound phase diagrams for Li_2O-Al_2O_3-B_2O_3-LiCl and Li_2S-Al_2S_3-B-S-LiCl systems are presented in Figs. 8 and 9 respectively, using data from Table VIII. These diagrams also offer insights into the starting materials necessary for the synthesis of specific target materials. For example, the synthesis of $Li_4B_7O_{12}Cl$ and $Li_6B_7O_{13}Cl$ would likely involve the precursors Li_2O, B_2O_3, and LiCl. Al-doped boracites can be obtained from the four binary materials located at the vertices of the phase diagram. Notably, the primary impurity phase, $LiAl_5O_8$—observed during the formation of $Li_4Al_3B_4O_{12}Cl$ by Kajihara *et al.* [4]—also appears in the phase diagram depicted in Fig. 8. For the case of thioboracites, $Li_6B_7S_{13}I$ [6] was experimentally identified using stoichiometric adjustments of Li_2S, B, S, and LiI [6]. Our calculations imply that a similar strategy is likely to work for obtaining $Li_4B_7S_{12}Cl$ and $Li_6B_7S_{13}Cl$, by using Li_2S, B, S, and LiCl as precursors. For forming Al-containing boracites, the incorporation of Al_2S_3 is suggested.

V. ESTIMATION OF VOLTAGE WINDOWS

Beyond equilibrium phase stability analysis, it is important to also consider the behavior of these materials in conditions found during battery operation. Several authors [37,39,43–48] have extended the ideas contributing to convex hull analyses to consider the effects of applied voltages and variable Li concentrations. In this case, the thermodynamics is characterized by the grand canonical potential, $\Omega(T, V, \{\mu_i\})$, which relates to the Helmholtz free energy through a Legendre transformation

$$\Omega(T, V, \{\mu_i\}) = F(T, V, \{N_i\}) - \sum_i N_i \mu_i. \tag{11}$$

Here N_i denotes the number of constituents of type i with μ_i denoting their corresponding chemical potential. These authors [37,39,43–45,48] and others developed a methodology to explore the convex hull for the grand canonical potential appropriate to these solid-state Li electrolytes. For the Li solid-state battery system, the focus is on variations in Li composition due to the thermodynamic driving forces acting on the solid electrolyte when in contact with Li reservoirs.

We can imagine a Li solid electrolyte as a reactant (R) with the possible addition of $n_{\rm Li}^a$ Li atoms from the anode reservoir such that phase equilibria (P) are formed. In this case, the reaction would be

$$\rm R + \it n_{\rm Li}^a \rm Li \rightarrow P. \tag{12}$$

On the other hand, we can imagine a Li solid electrolyte (R) possibly forming phase equilibria (P) while depositing $n_{\rm Li}^c$ Li atoms to the cathode reservoir,

$$\rm R \rightarrow P + \it n_{\rm Li}^c \rm Li. \tag{13}$$

In these two cases, there is a change in Li concentration $\Delta n_{\rm Li}$, which can be defined

$$\Delta n_{\rm Li} = \begin{cases} -n_{\rm Li}^a & \text{for case Eq. (12)} \\ +n_{\rm Li}^c & \text{for case Eq. (13)} \end{cases}. \tag{14}$$

In terms of the variable $\Delta n_{\rm Li}$, which signifies the possible addition of $n_{\rm Li}^a$ Li atoms from the anode reservoir or $n_{\rm Li}^c$ Li atoms from the cathode reservoir, we can approximate the grand canonical potential as

$$\Delta\Omega(\text{system}) \equiv F(\text{RHS}) - F(\text{LHS}) - \Delta n_{\rm Li}\mu_{\rm Li}. \tag{15}$$

Here RHS and LHS refer to reaction Eq. (12) or Eq. (13) as appropriate. For cases in which $\Delta n_{\rm Li} = 0$, R remains stable at $\mu_{\rm Li}$ such that P ≡ R, while for other cases, P may represent multiple compounds such as $\sum_i x_i \rm P_i$. As in Sec. IV, the Helmholtz free energies of the left (LHS) and right (RHS) sides of the reaction equations are assumed to be well represented by the static lattice internal energies $U_{SL}(\{N_i\})$ as in Eq. (1) on the optimized structure of each material and can be determined in terms of the formation energies defined in Eq. (7).

Following the work of Refs. [37,39,43–48], it is convenient to define a voltage-dependent (ϕ) Li chemical potential, $\mu_{\rm Li} \rightarrow \mu_{\rm Li}(\phi)$ according to

$$\mu_{\rm Li}(\phi) = \mu_{\rm Li}^0 - e\phi. \tag{16}$$

Here $\mu_{\rm Li}^0$ denotes the chemical potential of ideal Li metal representing a pure Li metal anode and e denotes the elementary charge. This expression is consistent with the analysis of Aydinol and coworkers [49] who analyzed the open circuit voltage $\phi^{\rm OCV}$ for a Li battery having Li chemical potentials $\mu_{\rm Li}^{\rm Cathode}$ at the cathode and $\mu_{\rm Li}^0$ at the anode,

$$e\phi^{\rm OCV} \equiv -\mu_{\rm Li}^{\rm Cathode} + \mu_{\rm Li}^0. \tag{17}$$

For a particular battery system under open circuit conditions, $\mu_{\rm Li}(\phi^{\rm OCV}) = \mu_{\rm Li}^{\rm Cathode}$ in Eq. (16). More generally, $\mu_{\rm Li}(\phi)$ in

TABLE II. For each of the eight most stable (thio)boracite electrolyte, the cathodic voltage ϕ_{CL} in units of volts (V) and the corresponding equilibrium phase compounds "CL phases", the anodic voltage ϕ_{AL} in units of volts (V) and the corresponding equilibrium phase compounds "AL phases" are listed. The last column lists the stability window ($\phi_{AL} - \phi_{CL}$) in units of volts (V).

Material	ϕ_{CL}	CL phases	ϕ_{AL}	AL phases	Window
$Li_4B_7O_{12}Cl$	1.491	$LiBO_2$, B_6O, LiCl	3.860	$Li_3B_7O_{12}$, Cl_2	2.369
$Li_6B_7O_{13}Cl$	1.357	$LiBO_2$, B_6O, LiCl	3.607	$Li_4B_7O_{12}Cl$, O_2	2.250
$Li_4Al_3B_4O_{12}Cl$	1.358	$LiBO_2$, B_6O, $LiAl_5O_8$, LiCl	3.629	$Li_4B_7O_{12}Cl$, LiCl, O_2, Al_2O_3	2.271
$Li_6Al_3B_4O_{13}Cl$	1.284	$LiBO_2$, B_6O, $LiAlO_2$	3.360	$LiBO_2$, $LiAl_5O_8$, LiCl, O_2	2.076
$Li_4B_7S_{12}Cl$	2.360	$Li_5B_7S_{13}$, BS, LiCl	2.491	BS_2, BS, LiCl	0.131
$Li_6B_7S_{13}Cl$	1.595	Li_2S, LiCl, B	2.454	BS_2, BS, LiCl	0.859
$Li_4Al_3B_4S_{12}Cl$	1.706	Li_5AlS_4, BS, Al_2S_3, LiCl	2.122	$Li_5B_7S_{13}$, Al_2S_3, LiCl, S	0.416
$Li_6Al_3B_4S_{13}Cl$	1.706	Li_5AlS_4, BS, Al_2S_3, LiCl	2.117	$Li_5B_7S_{13}$, Al_2S_3, LiCl, S	0.411

Eq. (16) allows for the exploration of possible cathode and voltage combinations for battery design and is what is used in Eq. (15). Moreover, since ideal Li metal is used as one of the reference elements in calculating the formation energies E_f according to Eq. (7), it is consistent to set $\mu^0_{\rm Li} = E_f({\rm Li}) = 0$. Consistent with this energy convention, the voltage and Li chemical potential are related by

$$e\phi = -\mu_{\rm Li}(\phi). \tag{18}$$

In these terms, we approximate the change in the grand canonical potential as

$$\Delta\Omega({\rm system}, \phi, \Delta n_{\rm Li}) = \Delta E_{gcp}({\rm system}) + \Delta n_{\rm Li} e\phi. \tag{19}$$

In this expression,

$$\Delta E_{gcp}({\rm system}) = 0 \quad \text{when} \quad \Delta n_{\rm Li} = 0, \tag{20}$$

and

$$\Delta E_{gcp}({\rm system}) \equiv \sum_i x_i N_{{\rm P}_i} E_f({\rm P}_i) - N_{\rm R} E_f({\rm R}) \quad \text{when} \quad \Delta n_{\rm Li} \neq 0. \tag{21}$$

In reporting values of $\Omega({\rm system}, \phi, \Delta n_{\rm Li})$, such as in Table IX, it is convenient to normalize the energies by the number $N_{\rm R}^{\rm NonLi}$ of non-Li atoms in the "reactant" electrolyte R. Accordingly, the normalized change in the grand canonical potential can be defined,

$$\overline{\Delta\Omega} \equiv \frac{\Delta\Omega}{N_{\rm R}^{\rm NonLi}}. \tag{22}$$

For a given solid electrolyte, exploring the change in the grand canonical potential $\Delta\Omega$ for a wide range of possible reaction products as a function of ϕ and $\Delta n_{\rm Li}$ indicates stability and reactivity information about the system based on its bulk thermodynamic energies. By this measure, the window of stability for the solid electrolyte is defined as the range of values of the potential ϕ [and the corresponding ranges of chemical potentials $-\mu_{\rm Li}(\phi)$] for $\Delta\Omega({\rm system}, \phi, \Delta n_{\rm Li}) = 0$. Conditions that produce $\Delta\Omega < 0$ indicate that a spontaneous decomposition or the exchange Li with the anode or cathode reservoir is predicted to occur. A number of voltage window estimates for electrolytes have appeared in the literature [43–45,50]. Typically the range is found to be $0 \leqslant \phi \leqslant 5$ V. The lower value ϕ_{CL} ("cathodic limit" in the chemistry literature) represents the lowest voltage at which Li from that anode ceases to react with the electrolyte ($n^a_{\rm Li} \to 0$). The upper value of ϕ_{AL} ("anodic limit" in the chemistry literature) of the range of $\Delta\Omega({\rm system}, \phi, \Delta n_{\rm Li}) = 0$ represents the highest voltage before which Li from the cathode starts to react with the electrolyte ($0 \to n^c_{\rm Li}$). Using the Pymatgen software package [39], we examined the grand canonical potential phase diagrams of the eight most stable (thio)boracite electrolytes over a voltage range of $0\ {\rm V} \leqslant \phi \leqslant 5$ V, with values distributed uniformly. A graphical representation of the results for the voltage windows are presented in Fig. 10, while the corresponding numerical data can be found in Table II. Further results are detailed in Appendix C. Table IX presents the complete reaction equations, accompanied by their respective normalized decomposition reaction energies $\overline{\Delta\Omega}(\phi)$ at transition voltages/Li chemical potentials. Meanwhile, Table X lists the $\overline{\Delta\Omega}(\phi)$ energies at the extreme voltages of $\phi = 0$ V and $\phi = 5$ V.

As illustrated in Fig. 10, the voltage windows of thioboracite materials are found to be relatively narrow and fall within the range of their thioboracite analogues. This observation is consistent with previous studies, indicating suboptimal voltage windows in sulfide-based electrolytes compared to oxide-based alternatives [51,52]. Specifically, boracite materials define a stability window from 2.076 V to 3.369 V. In contrast, thioboracite derivatives display a range 0.131–0.859 V. Among the studied materials, $Li_4B_7S_{12}Cl$

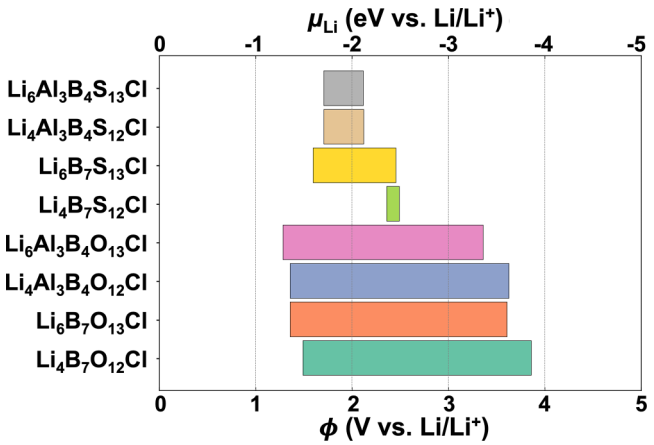

FIG. 10. The electrochemical stability ranges of (thio)boracites electrolyte materials, generated using the data summarized in Table II.

demonstrates the most constrained window with a value of 0.131 V. This observation can be ascribed to the persistent presence of $Li_5B_7S_{13}$—a notably stable phase - in the decomposition products of $Li_4B_7S_{12}Cl$ throughout the examined voltage range. Further analysis, detailed in Appendix C and Table X, suggests that upon reacting with bulk Li metal at $\phi = 0$ V, the reaction energies $\overline{\Delta\Omega}(\phi)$ of thioboracite materials were found to be lower than those of boracite materials, implying that thioboracite materials are comparatively less stable in contact with pure Li metal. A similar trend was observed at a $\phi = 5$ V cathode side, where a comparatively larger driving force for the decomposition of thioboracite materials was noted. However, during the delithiation reaction at high voltages, all boracite materials exhibit the release of gas-phase decompositions of O_2 and/or Cl_2, which may pose significant challenges to the long-term stability of the electrolyte. It is also found that the doping of Al in pure (thio)boracites does not appear to enhance the electrochemical window, except for the case of $Li_4B_7S_{12}Cl$ and $Li_4Al_3B_4S_{12}Cl$, which could be due to the aforementioned reason. The relatively narrow stability windows of Al-doped materials are likely due to the presence of Al-containing compounds in the decomposition products.

When comparing computational results with experimental characterizations, clear discrepancies emerge. for example, the calculated electrochemical stability windows for $Li_4B_7O_{12}Cl$ and $Li_4Al_3B_4O_{12}Cl$ are 2.369 V and 2.271 V, respectively. However, experimental data shows that $Li_4B_7O_{12}Cl$ has a measured electrochemical stability window extending up to 4.3 V [2], while $Li_4Al_3B_4O_{12}Cl$ spans from 0 to 6 V [4]. The lack of agreement can largely be attributed to the passivating effects evidenced in previous studies [43,44,53]. As shown in Table IX, the (thio)boracite materials rarely generate metallic compounds during the reactions (LiB_3 are zero-gap semiconductors [54]). This characteristic implies that these materials may become passivated by forming decomposition products with poor electronic conductivity upon contact with electrodes over an extended voltage range. The formation of passivating products can potentially prevent further degradation of the electrolyte, maintaining optimal electrochemical performance. As a result, the (thio)boracite materials, when synthesized with equilibrium phases, are expected to deliver an electrochemical window that surpasses their inherent intrinsic capacities.

VI. ANALYSIS OF HARMONIC PHONONS OF THE (THIO)BORACITES BASED ON THE IDEALIZED GROUND-STATE STRUCTURES

Omitted from our analysis so far is the consideration of lattice vibrations, which are important for understanding the dynamic stabilities of the materials and for estimating temperature dependent contributions to the Helmholtz free energy. Here we focus on the harmonic approximation, omitting consideration of anharmonic effects. An improvement over Eq. (1) to the estimate of the Helmholtz free energy of a system composed of N_i atoms of type i at temperature T and volume V is given by

$$F(T, V, \{N_i\}) = U_{SL}(\{N_i\}) + F_{\rm vib}(T, V, \{N_i\}). \tag{23}$$

The vibrational contribution to the Helmholtz free energy depends on the frequencies of the normal modes ν of vibration $\omega_\nu(\mathbf{q})$, as a function of phonon wavevector $\mathbf{q}$ sampled throughout the Brillouin zone with weight factors $W(\mathbf{q})$ according to [55]

$$F_{\rm vib}(T, V, \{N_i\}) = k_B T \sum_{\nu\mathbf{q}} W(\mathbf{q}) \left(\ln\left(2\sinh\left(\frac{\hbar\omega_\nu(\mathbf{q})}{2k_B T} \right) \right) \right), \tag{24}$$

where $\hbar$ and k_B denote the Planck and Boltzmann constants, respectively. In order to evaluate Eq. (24) quantitatively as well as to evaluate the phonon band structure and the phonon densities of states, it is necessary to determine the normal mode frequencies $\omega_\nu(\mathbf{q})$ on a reasonably dense $\mathbf{q}$-point grid throughout the Brillouin zone (typically $16 \times 16 \times 16$ sampling points along the three vectors of the reciprocal lattice of the primitive cell). From the pioneering study of Giannozzi, Gonze, and others [10–14], density functional perturbation theory (DFPT) can be used to find the dynamical matrix as a function of $\mathbf{q}$. For computational efficiency, DFPT is used with a relatively coarse $\mathbf{q}$-point sampling ($2 \times 2 \times 2$ or $4 \times 4 \times 4$ sampling points) together with symmetry analysis. These results are then used with Fourier analysis to find the real-space force-constant matrix. This real-space force-constant matrix is then used to find the dynamical matrix and normal mode frequencies $\omega_\nu(\mathbf{q})$ on a $\mathbf{q}$-point grid. This methodology is available in the ABINIT and QUANTUM ESPRESSO packages and in our tests on a few of the systems, we find good agreement between the codes ($\Delta F_{\rm vib}(T, V, \{N_i\}) = \pm 0.01$ eV/FU) when the coarse $\mathbf{q}$-point sampling is well converged. However, we note that variations in the computation of $F_{\rm vib}(T, V, \{N_i\})$ can be much larger (± 0.04 eV/FU for example) when the coarse $\mathbf{q}$-point sampling is not well converged. Another approach, based evaluating the real-space force-constant matrix from finite displacements of the equilibrium atoms within supercells, [56] has been implemented by Togo and coworkers in the PHONOPY code [57,58]. For systems with relatively large primitive cells ($\approx$54 atoms for the Li_6 (thio)boracites), some having low symmetry, we find PHONOPY to be computationally efficient, using QUANTUM ESPRESSO to evaluate the forces in the supercell and also to evaluate the long-range dipolar electric field couplings [10,11,59] using DFPT at $\mathbf{q} = 0$. It is our experience that relatively small supercells ($2 \times 2 \times 2$ multiples of the primitive lattice vectors for the eight Li (thio)boracites and $4 \times 4 \times 4$ multiples of the primitive lattice vectors of Li_2O and Li_2S) give reasonable results. The phonon analysis reported here was generated using this approach.

Using Eq. (24), it is possible to analyze the temperature-dependent energetics of the harmonic phonon contributions to the Helmholtz free energy. Of interest is to measure the magnitude of the vibrational energy, which have been neglected in estimating the equilibrium phase diagrams and in estimating the grand canonical potential analysis. Following the approach of Sec. (III), it is convenient to define free energy differences again based on the Li_4boracite material in the $R3c$ structure. For family members having the Li_4 stoichiometries,

TABLE III. Summary of results for $\Delta F(T, V, \{N_i\})$ in units of eV/formula unit as estimated from Eqs. (25) and (26), referenced to the corresponding Li_4 boracite in its $R3c$ structure plus Li_2O or Li_2S, as appropriate, calculated at temperatures $T = 0$, 300, and 400 K.

Formula	SG	ΔF $T = 0$ K	ΔF $T = 300$ K	ΔF $T = 400$ K
$Li_4B_7O_{12}Cl$	$R3c$	0.00	0.00	0.00
$Li_6B_7O_{13}Cl$	$R3c$	−1.59	−1.53	−1.50
$Li_6B_7O_{13}Cl$	Cc	−1.27	−1.22	−1.20
$Li_4Al_3B_4O_{12}Cl$	$R3c$	0.00	0.00	0.00
$Li_6Al_3B_4O_{13}Cl$	$R3c$	−0.25	−0.20	−0.18
$Li_6Al_3B_4O_{13}Cl$	Cc	−0.42	−0.35	−0.32
$Li_4B_7S_{12}Cl$	$R3c$	0.00	0.00	0.00
$Li_4B_7S_{12}Cl$	$F\bar{4}3c$	−0.07	−0.09	−0.10
$Li_6B_7S_{13}Cl$	$R3c$	−0.96	−0.92	−0.89
$Li_6B_7S_{13}Cl$	Cc	−1.05	−0.99	−0.96
$Li_4Al_3B_4S_{12}Cl$	$R3c$	0.00	0.00	0.00
$Li_6Al_3B_4S_{13}Cl$	$R3c$	−0.33	−0.23	−0.19
$Li_6Al_3B_4S_{13}Cl$	Cc	−0.63	−0.52	−0.47

$\Delta F(T, \text{Li}_4\text{boracite})$ is defined as

$$\Delta F(T, \text{Li}_4\text{boracite}) \equiv F(T, \text{Li}_4\text{boracite})) - F(T, \text{Li}_4\text{boracite}[R3c]). \quad (25)$$

For family members having the Li_6 stoichiometries, $\Delta F(T, \text{Li}_6\text{boracite})$ is defined as

$$\Delta F(T, \text{Li}_6\text{boracite}) \equiv F(T, \text{Li}_6\text{boracite}) - F(T, \text{Li}_4\text{boracite}[R3c]) - F(T, \text{Li}_2\text{X}). \quad (26)$$

Here Li_2X denotes Li_2O or Li_2S as appropriate. Table III lists $\Delta F(T, V, \{N_i\})$ accordingly, calculated at temperatures $T = 0, 300$, and 400 K. Here we see that the vibrational contributions to the Helmholtz free energy contributions are less than 0.03 eV/FU at $T = 0$ K and less than 0.08 eV/FU at $T = 300$ K, small enough to predict the same phase stability patterns as the static lattice energies given in Table I. Of the 16 materials listed in Table I, only the 13 materials with negative static lattice energies ΔU_{SL} are included in Table III (omitting three of the Li_4 materials with the ordered $F\bar{4}3c$ structures).

In performing the analysis of the normal mode spectra of the 13 materials, we find that, with one exception, all are dynamically stable by the criterion of finding no imaginary modes. The exception is $Li_6B_7S_{13}Cl$ in the $R3c$ structure, which is found to have some imaginary modes in a small volume of the Brillouin zone near $\mathbf{q} = 0$. The volume of phase space, which contributes to these imaginary modes is so small as to have a negligible numerical contribution to the phonon density of states, but nevertheless indicates some dynamic instability of this structure. The normal mode band diagrams together with partial densities of states profiles of all 13 materials are given in the of the Part I of the SM [36], while those of the eight most stable structures are presented here. Here, to represent the phonon band dispersions of the normal mode frequencies $\omega_\nu(\mathbf{q})$, we use the "standard" Brillouin zone paths for the $F\bar{4}3c$, $R3c$, and Cc structures established by

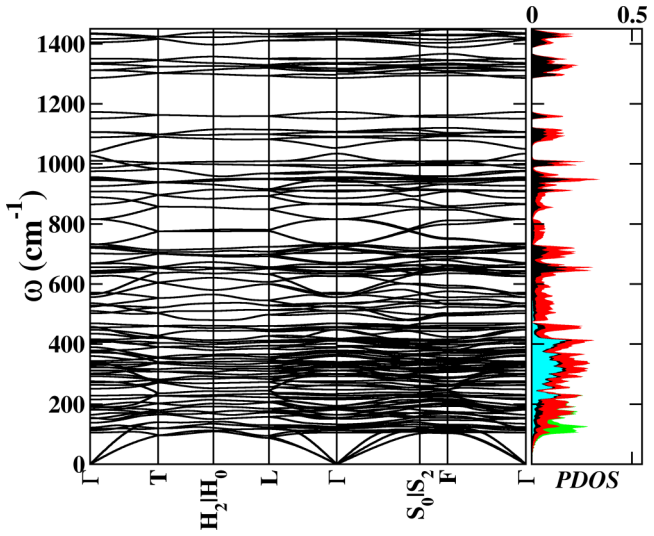

FIG. 11. Phonon bands and densities of states for $Li_4B_7O_{12}Cl$ in the $R3c$ structure.

Hinusa *et al.* [60], which are reproduced in the Appendix D in Fig. 19. Additionally, the partial densities of states $g_a(\omega)$, calculated from the normal mode eigenstates for each atom type a as given, for example, in Eq. (13) of Ref. [22], are also visualized. In this paper, $g_a(\omega)$ is calculated by representing the δ function as a normalized Gaussian function with a smearing width of 1.7 cm^{-1} as calculated within the PHONOPY code. The total density of phonon states $g(\omega)$ is given as the sum of the partial density of states contributions,

$$g(\omega) = \sum_a g_a(\omega). \quad (27)$$

In the following figures, the phonon frequencies are given in units of cm^{-1}. The side panel presents the phonon densities of states $g(\omega)$ in units of (states per unit cell)/cm^{-1} as indicated with the full curve. Within the full curve, the

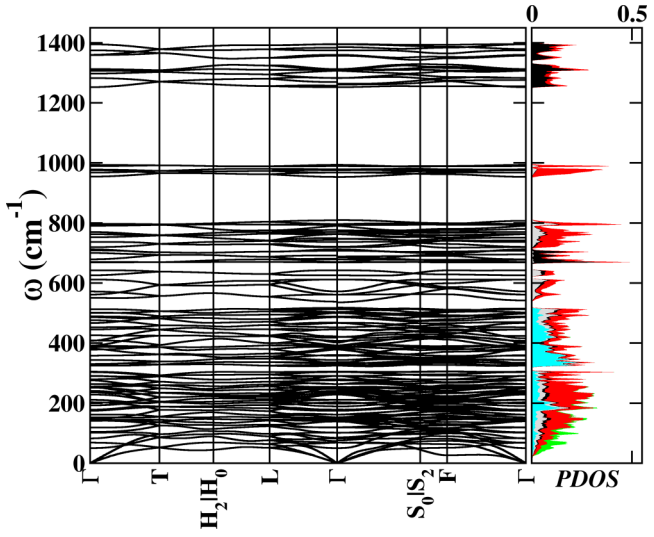

FIG. 12. Phonon bands and densities of states for $Li_4Al_3B_4O_{12}Cl$ in the $R3c$ structure.

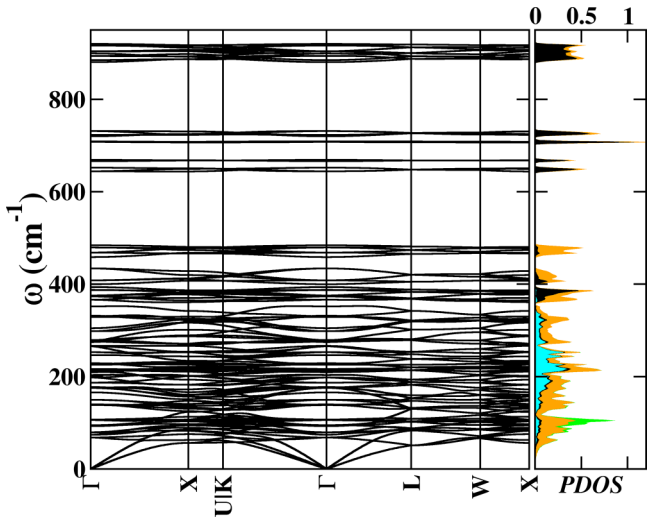

FIG. 13. Phonon bands and densities of states for $Li_4B_7S_{12}Cl$ in the $F\bar{4}3c$ structure.

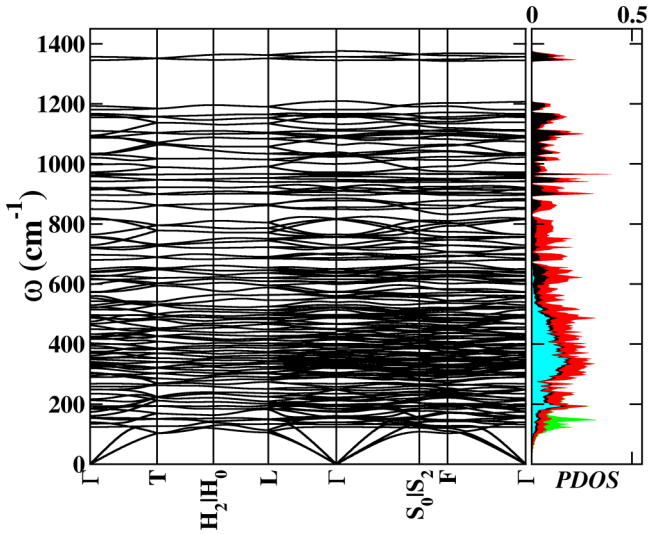

FIG. 15. Phonon bands and densities of states for $Li_6B_7O_{13}Cl$ in the $R3c$ structure.

partial density of states components $g_a(\omega)$ are represented by shaded segments; the width at each ω indicating the magnitude of $g_a(\omega)$. The curve segments are presented in the following order: Li (light blue), Al (grey, if present), B (black), O (red) or S (orange), and Cl (green). The phonon spectrum of the most stable Li (thio)boracites are presented in Figs. 11–18, representing $Li_4B_7O_{12}Cl$ in the $R3c$ structure, $Li_4Al_3B_4O_{12}Cl$ in the $R3c$ structure, $Li_4B_7S_{12}Cl$ in the $F\bar{4}3c$ structure, $Li_4Al_3B_4S_{12}Cl$ in the $R3c$ structure, $Li_6B_7O_{13}Cl$ in the $R3c$ structure, and $Li_6Al_3B_4O_{13}Cl$, $Li_6B_7S_{13}Cl$, and $Li_6Al_3B_4S_{13}Cl$ all in the Cc structure, respectively. The phonon band diagrams and phonon partial density of states for all of the 13 Li (thio)boracites listed in Table III are given in Sec. III of Part I of the SM [36]. (Note that in this section of the manuscript and in the corresponding section of the SM, the label "PDOS" refers to the phonon partial density of states.)

These phonon band diagrams have some interesting features. For example, the Li contributions are generally confined to the low-frequency range of $0 \leqslant \omega \leqslant 500 - 600$ cm^{-1}. As the most massive ion in the Li (thio)boracite family, the Cl vibrational contributions are confined to small frequencies less than 200 cm^{-1}. Both O and S contribute throughout the phonon spectrum, participating both in modes associated with Li and Cl ions in the void regions and in the framework modes due to localized vibrations of the BO_4, AlO_4, BS_4, and AlS_4 tetrahedra and the BO_3 and BS_3 triangular framework components. The triangular planar structures are responsible for the highest frequency modes for all of the Li boracite materials and for the Li_4 thioboracites. Since Al is more massive than B, it is not surprising that the framework modes associated with the AlO_4 and AlS_4 tetrahedral units generally occur at lower frequencies than those of the BO_4 and BS_4 tetrahedral units. It is interesting to note that of the 13 stable and metastable

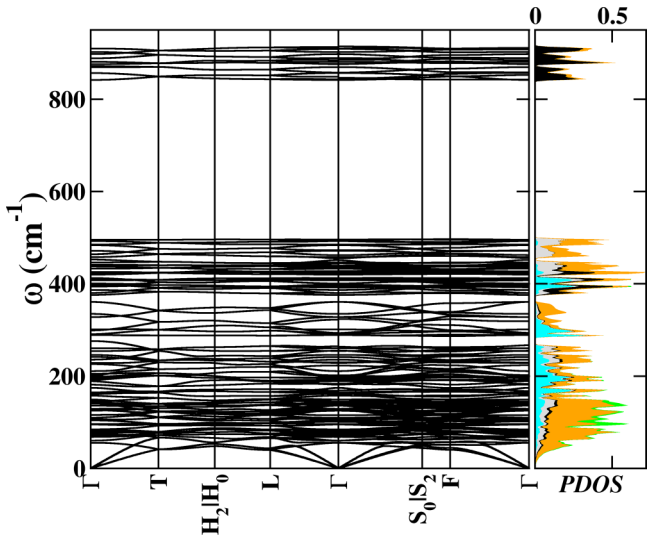

FIG. 14. Phonon bands and densities of states for $Li_4Al_3B_4S_{12}Cl$ in the $R3c$ structure.

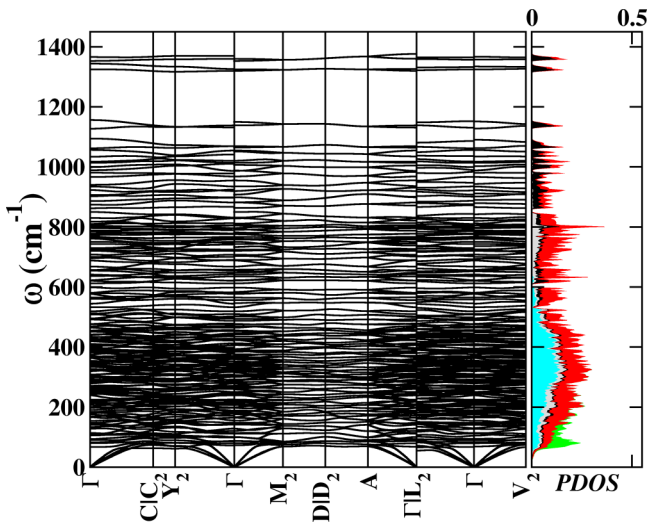

FIG. 16. Phonon bands and densities of states for $Li_6Al_3B_4O_{12}Cl$ in the Cc structure.

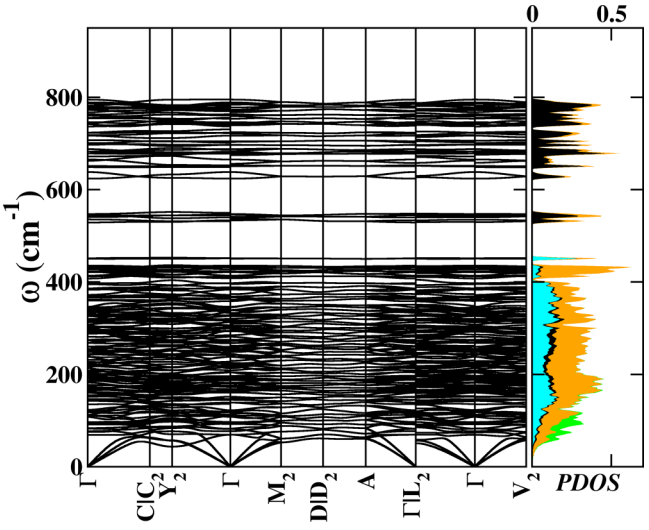

FIG. 17. Phonon bands and densities of states for $Li_6B_7S_{12}Cl$ in the *Cc* structure.

structures considered in this paper, only $Li_6B_7S_{13}Cl$ in the *R*3*c* crystalline form shows evidence of imaginary phonon frequencies. As shown in Fig. 8 of Part I of the SM [36], these imaginary modes occur in a small volume of the Brillouin zone near $\mathbf{q} = 0$. Interestingly, as discussed in Sec. III, this material shows considerable similarity to $Li_6B_7S_{13}I$ found experimentally by Kaup and coworkers [6] in the disordered $F\bar{4}3c$ structure. It is possible that the halide iodine contributes some dynamic stabilization compared with chlorine or that the simulations are missing significant properties of the real materials [61]. On the other hand, the related monoclinic structure (*Cc*; No. 9) of $Li_6B_7S_{13}Cl$ and of several of the other Li_6 (thio)boracites is computational predicted to be more stable by 0.1 eV/FU or more and are all predicted to be dynamically stable. To our knowledge, these *Cc* structures have not yet been reported in the experimental literature.

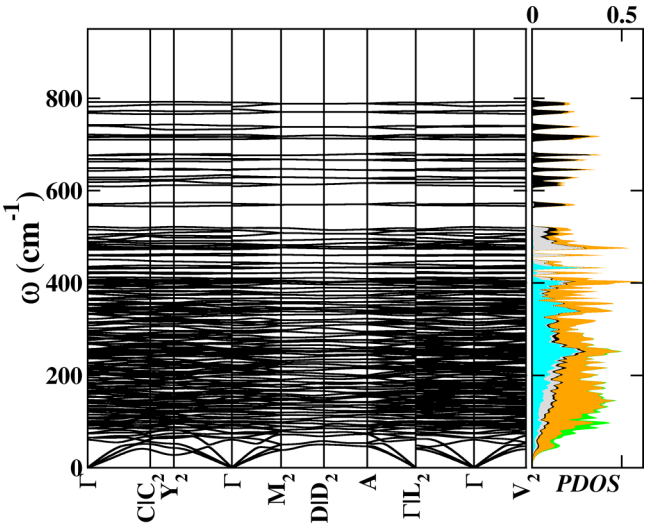

FIG. 18. Phonon bands and densities of states for $Li_6Al_3B_4S_{12}Cl$ in the *Cc* structure.

VII. SUMMARY AND CONCLUSIONS

In this paper we have built upon previous computational and experimental investigations regarding known materials ($Li_4B_7O_{12}Cl$, $Li_4Al_3B_4O_{12}Cl$, and $Li_6B_7S_{13}I$) and extended this family of (thio)boracites to include newly predicted materials based on our computational efforts ($Li_4B_7S_{12}Cl$, $Li_4Al_3B_4S_{12}Cl$, $Li_6B_7O_{13}Cl$, $Li_6Al_3B_4O_{13}Cl$, $Li_6B_7S_{13}Cl$, and $Li_6Al_3B_4S_{13}Cl$).

We have discovered new structures apart from the previously known ordered *R*3*c* and disordered $F\bar{4}3c$ phases, namely new ordered *Cc* and $F\bar{4}3c$ structures. For the Li_4 family of materials we have investigated, we have determined that the energetically favorable ground states for all materials prefer the *R*3*c* structure, except the computationally predicted $Li_4B_7S_{12}Cl$, which has a lowest-energy state in the $F\bar{4}3c$ structure, with fully occupied Li 32e sites in the conventional cell. For the Li_6 materials, we have found a different pattern, that they all energetically favor the *Cc* structure, except for the computationally predicted $Li_6B_7O_{13}Cl$, which has a lowest-energy structure with *R*3*c* symmetry.

We have adopted several methodologies for investigating the stability of these materials, including convex hull analysis of the composition spaces of Li-Al-B-O-Cl and Li-Al-B-S-Cl, estimation of voltage windows in practical applications, and phonon mode analysis.

The convex hull analysis suggests that the $Li_4B_7O_{12}Cl$ material is the only one that is chemically stable, but this is not quite the full story. Materials with very small positive values of hull energy may be stable, or at the very least metastable. For example, the experimentally synthesized and investigated $Li_4Al_3B_4O_{12}Cl$ is computed to have the small positive hull energy of 0.053 eV/atom. This small unexpected positive energy may be caused by the limited accuracy of density functional calculations or by the simplifying approximations to the physical system made in the analysis. The sensitivity of the results to the choice of the exchange-correlation functional may be worth examining in future work. While the PBEsol functional [16] has been successfully used in our previous work [22] and by many other authors [62], new functionals appearing in the more recent literature may possibly predict a slightly different phase diagram.

The voltage window analysis attempts to model real world stability of these materials when placed in contact with a pure Li metal anode and with a voltage applied across the solid electrolyte. The results from this model suggest that all of the oxygen-based materials have good stability in contact with Li metal, whereas the sulfur-based materials do not. The low stability in contact with Li metal found here does not preclude the thioboracites from being useful in practice, as this may be addressable with anode coatings and/or by using another anode that is not pure Li.

From the phonon calculations, we have generated the vibrational energies at 0 K, 300 K, and 400 K, and these data points further solidify our previous ground-state predictions from the static lattice energies alone. The phonon modes themselves also indicate vibrational stability of our ground-state structures, as they all have real frequencies. The only structure investigated that was found to have instability as indicated by imaginary phonon modes was $Li_6B_7S_{13}Cl$ in its

TABLE IV. Conventional cell fractional coordinates of $Li_4B_7O_{12}Cl$ from the optimized structure (face-centered $R3c$) compared with the experimental structure at room temperature (face-centered-cubic $F\bar{4}3c$) reported in Ref. [5]. The corresponding lattice parameters are given in Table I. The "Label" columns with notation 8/32*e* give the (number of occupied sites)/(site multiplicity)(Wyckoff label) for the appropriate space group. The multiplicity for each listed site includes the full face-centered translations of (0, 0, 0), ($\frac{1}{2}$, $\frac{1}{2}$, 0), (0, $\frac{1}{2}$, $\frac{1}{2}$), and ($\frac{1}{2}$, 0, $\frac{1}{2}$).

Atom	Label	(x, y, z) for $R3c$	Label	(x, y, z) for $F\bar{4}3c$
Li	24/24*b*	(0.035,0.251,0.250)	24/24*c*	(0.000,0.250,0.250)
Li	8/8*a*	(0.369,0.369,0.369)	8/32*e*	(0.361,0.361,0.361)
B	24/24*b*	(0.256,0.007,0.002)	24/24*d*	(0.250,0.000,0.000)
B	8/8*a*	(0.102,0.102,0.102)	32/32*e*	(0.101,0.101,0.101)
B	24/24*b*	(0.903,0.903,0.109)		(0.899,0.899,0.101)
O	24/24*b*	(0.026,0.097,0.185)	96/96*h*	(0.022,0.099,0.182)
O	24/24*b*	(0.979,0.901,0.193)		(0.978,0.901,0.182)
O	24/24*b*	(0.981,0.106,0.822)		(0.978,0.099,0.818)
O	24/24*b*	(0.024,0.909,0.827)		(0.022,0.901,0.818)
Cl	8/8*a*	(0.250,0.250,0.250)	8/8*b*	(0.250,0.250,0.250)

$R3c$ structure, while in its ground-state Cc structure, all of the phonon modes are real.

The predicted materials investigated in this paper seem quite promising and it seems plausible that there are viable routes of synthesis for these materials and that they may be metastable with respect to their precursors. This paper has established the structures and stability of this very intriguing family of (thio)boracites, but more investigation is needed to determine other properties. Future work is planned to investigate more of these properties, such as ionic conductivity, electrolyte performance, and ion migration mechanisms.

ACKNOWLEDGMENTS

The work by D.C.L., Y.L., and N.A.W.H. was supported by NSF Grants No. DMR-1940324 and No. DMR-2242959; the work by Y.L. and P.C. was supported by the National Research Foundation, Singapore under the NRF Fellowship NRFF12-2020-0012. Computations were performed using the Wake Forest University (WFU) High Performance Computing Facility, a centrally managed computational resource available to WFU researchers including faculty, staff, students, and collaborators. We would like to specially thank Dr. Sean Anderson for help with the software on the WFU-HPC computer system. We also like to thank Prof. Stephen Winter and Dr. Saif Ullah at WFU for their helpful comments.

APPENDIX A: TABLES OF FRACTIONAL COORDINATES

In this Appendix we list the computed fractional coordinates of the optimized structures described in Sec. III of this paper, compared with experimental results from the literature when available. The listed coordinates are chosen among their equivalents so that the relationships between the materials can be compared, but of course are not unique. The full primitive cell coordinates from which these results are provided in the Part I of the SM [36].

In Table IV we list the computed $R3c$ fractional coordinates of the optimized structure of $Li_4B_7O_{12}Cl$ slightly updated from the previously reported in Ref. [3] and compared with

TABLE V. Conventional cell fractional coordinates of $Li_4Al_3B_4O_{12}Cl$ from the optimized structure (face-centered $R3c$) compared with the experimental structure at room temperature (face-centered-cubic $F\bar{4}3c$) reported in Ref. [5]. The notation is the same as that in Table IV.

Atom	Label	(x, y, z) for $R3c$	Label	(x, y, z) for $F\bar{4}3c$
Li	24/24*b*	(0.963,0.223,0.223)	24/24*c*	(0.000,0.250,0.250)
Li	8/8*a*	(0.354,0.354,0.354)	8/32*e*	(0.364,0.364,0.364)
Al	24/24*b*	(0.225,0.980,0.979)	24/24*d*	(0.250,0.000,0.000)
B	8/8*a*	(0.086,0.086,0.086)	32/32*e*	(0.106,0.106,0.106)
B	24/24*b*	(0.871,0.871,0.081)		(0.894,0.894,0.106)
O	24/24*b*	(0.008,0.091,0.155)	96/96*h*	(0.027,0.109,0.178)
O	24/24*b*	(0.950,0.865,0.152)		(0.973,0.891,0.178)
O	24/24*b*	(0.947,0.089,0.800)		(0.973,0.109,0.822)
O	24/24*b*	(0.996,0.870,0.804)		(0.027,0.891,0.822)
Cl	8/8*a*	(0.250,0.250,0.250)	8/8*b*	(0.250,0.250,0.250)

TABLE VI. Conventional cell fractional coordinates of $Li_6B_7S_{13}Cl$ from the optimized structure (face-centered $R3c$) compared with the corresponding coordinates of $Li_6B_7S_{13}I$ reported in the supplemental materials of Ref. [6], shifted by $(\frac{1}{2}, \frac{1}{2}, \frac{1}{2})$, for the $F\bar{4}3c$ structure. The notations is the same that given in IV.

Atom	Label	$R3c$ (x, y, z)	Label	$F\bar{4}3c$ (x, y, z)
Li	24/24*b*	(0.087,0.250,0.252)	16/24*c*	(0.000,0.250,0.250)
Li	24/24*b*	(0.889,0.880,0.163)	32/32*e*	(0.859,0.859,0.141)
B	24/24*b*	(0.271,0.021,0.018)	24/24*d*	(0.250,0.000,0.000)
B	8/8*a*	(0.443,0.443,0.443)	32/32*e*	(0.423,0.423,0.423)
B	24/24*b*	(0.598,0.596,0.443)		(0.577,0.577,0.423)
S	24/24*b*	(0.038,0.202,0.412)	96*h*	(0.014,0.181,0.395)
S	24/24*b*	(0.007,0.839,0.415)		(0.986,0.819,0.395)
S	24/24*b*	(0.031,0.840,0.626)		(0.014,0.819,0.605)
S	24/24*b*	(0.005,0.201,0.623)		(0.986,0.181,0.605)
S	8/8*a*	(0.020,0.020,0.020)	8/8*a*	(0.000,0.000,0.000)
Cl/I	8/8*a*	(0.250,0.250,0.250)	8/8*b*	(0.250,0.250,0.250)

the recent literature results of Ref. [5] in the basis of the conventional face-centered unit cells. In Table V the computed optimized $R3c$ fractional coordinates of $Li_4Al_3B_4O_{12}Cl$ are listed and compared with the recent literature results of Ref. [5] in the basis of the conventional face-centered unit cells. In Table VI the computed optimized $R3c$ fractional coordinates of $Li_6B_7S_{13}Cl$ are listed and compared with the literature results for cubic $Li_6B_7S_{13}I$ reported in Ref. [6] in the basis of the conventional face-centered unit cells. In Table VII the computed optimized $R3c$ fractional coordinates of $Li_6B_7O_{13}Cl$ and $Li_6Al_3B_4O_{13}Cl$ are listed in the basis of the conventional face-centered unit cells.

APPENDIX B: FORMATION ENERGIES AND CONVEX HULL ANALYSIS FOR MATERIALS RELATED TO THE LI (THIO)BORACITE FAMILY

This appendix presents in Table VIII the essential data used to generate the phase diagrams in Figs. 8 and 9. This includes the reduced formula form of each material in column 2. In cases where a material has multiple phases, only the lowest-energy phases are included in the table, with symmetry information (space group symbol and number in the bracket [30]) given in column 3. Detailed structural information for these lowest-energy structures are available in the Part II of the SM [36].

APPENDIX C: ENERGY TABLES RELATED TO THE ANALYSIS OF THE VOLTAGE STABILITY OF LI (THIO)BORACITE FAMILY

Tables IX and X list some of the details of the analysis of the grand canonical potential for the Li (thio)boracites.

APPENDIX D: "STANDARD" BRILLOUIN ZONE PATHS AND LABELS

For convenience we present in Fig. 19 the recommended Brillouin zone labels and paths according to Ref. [60] used in the phonon band diagrams of this paper. This choice is an update of the previous study of Setyawan and Curtarola [65].

TABLE VII. Conventional cell-fractional coordinates (x, y, z) of $Li_6B_7O_{13}Cl$ from the optimized structure (face-centered $R3c$) compared with the corresponding coordinates for $Li_6Al_3B_4O_{13}Cl$. The notations is the same that given in Table IV.

Atom	Label	$Li_6B_7O_{13}Cl$	$Li_6Al_3B_4O_{13}Cl$
Li	24/24*b*	(0.036,0.241,0.238)	(0.039,0.238,0.245)
Li	24/24*b*	(0.875,0.870,0.139)	(0.889,0.872,0.141)
B	24/24*b*	(0.255,0.003,0.004)	(0.270,0.015,0.005)
B	8/8*a*	(0.403,0.403,0.403)	(0.421,0.421,0.421)
B/Al	24/24*b*	(0.585,0.584,0.430)	(0.601,0.592,0.431)
O	24/24*b*	(0.096,0.019,0.329)	(0.924,0.994,0.342)
O	24/24*b*	(0.024,0.185,0.408)	(0.114,0.013,0.323)
O	24/24*b*	(0.982,0.898,0.821)	(0.991,0.217,0.605)
O	24/24*b*	(0.978,0.191,0.603)	(0.913,0.023,0.704)
O	8/8*a*	(0.016,0.016,0.016)	(0.023,0.023,0.023)
Cl	8/8*a*	(0.250,0.250,0.250)	(0.250,0.250,0.250)

TABLE VIII. Results for compounds in the Li-B-Al-O-Cl and Li-B-Al-S-Cl systems assessed in this study. The "Formation" and "Hull" columns provide the formation energy [calculated based on Eq. (7)] and the energy above the hull [calculated using Eq. (8) to Eq. (10)], respectively, for each compound listed in the second column. The "Equilibrium" column specifies the equilibrium phases with their corresponding stoichiometric coefficients. All energy values are presented in eV/atom. Note that entry #65 for $Li_{7.5}B_{10}S_{18}Cl_{1.5}$ was based on the material reported in Ref. [63], using the crystal structure described in Ref. [64].

No.	Material	Symmetry	Formation	Hull	Equilibrium
1	Li	$Im\bar{3}m(229)$	0.000	0.000	1.00 Li
2	Al	$F3m3(225)$	0.000	0.000	1.00 Al
3	B	$R\bar{3}m(166)$	0.000	0.000	1.00 B
4	S	$P2/c(13)$	0.000	0.000	1.00 S
5	O ($\frac{1}{2}$ O_2)	$C2/m(12)$	0.000	0.000	1.00 O
6	Cl ($\frac{1}{2}$ Cl_2)	$Cmce(64)$	0.000	0.000	1.00 Cl
7	Li_9Al_4	$C2/m(12)$	−0.111	0.036	4.00 Li_2Al + 1.00 Li
8	LiAl	$I4_1/amd(141)$	−0.176	0.000	1.00 LiAl
9	$LiAl_3$	$Pm\bar{3}m(221)$	−0.089	0.000	1.00 $LiAl_3$
10	Li_2Al	$Cmcm(63)$	−0.159	0.000	1.00 Li_2Al
11	Li_3Al_2	$R\bar{3}m(166)$	−0.123	0.043	1.00 Li_2Al + 1.00 LiAl
12	LiB_3	$P4/mbm(127)$	−0.216	0.000	1.00 LiB_3
13	Li_5B_4	$Cm(8)$	0.150	0.278	1.33 LiB_3 + 3.67 Li
14	LiB	$P6_3/mmc(194)$	−0.124	0.021	0.33 LiB_3 + 0.67 Li
15	Li_2S	$Fm\bar{3}m(225)$	−1.366	0.000	1.00 Li_2S
16	Li_2O	$Fm\bar{3}m(225)$	−1.842	0.000	1.00 Li_2O
17	Li_2O_2	$P6_3/mmc(194)$	−1.416	0.000	1.00 Li_2O_2
18	LiCl	$Fm\bar{3}m(225)$	−1.843	0.000	1.00 LiCl
19	AlB_2	$P6/mmm(191)$	−0.072	0.000	1.00 AlB_2
20	AlB_{12}	$P4_12_12(92)$	0.336	0.353	1.00 AlB_2 + 10.00 B
21	Al_2S_3	$I4_1/amd(141)$	−1.121	0.000	1.00 Al_2S_3
22	Al_2O_3	$R\bar{3}c(167)$	−3.062	0.000	1.00 Al_2O_3
23	$AlCl_3$	$C2/m(12)$	−1.549	0.000	1.00 $AlCl_3$
24	BS	$R\bar{3}m(166)$	−0.452	0.000	1.00 BS
25	BS_2	$P2_1/c(14)$	−0.367	0.000	1.00 BS_2
26	B_2S_3	$P2_1/c(14)$	−0.395	0.006	1.00 BS_2 + 1.00 BS
27	B_6O	$R\bar{3}m(166)$	−0.715	0.000	1.00 B_6O
28	B_2O_3	$Cmc2_1(36)$	−2.414	0.000	1.00 B_2O_3
29	BCl_2	$Pbca(61)$	−0.701	0.127	0.50 BCl + 0.50 BCl_3
30	BCl	$Pa\bar{3}(205)$	−0.629	0.000	1.00 BCl
31	BCl_3	$P6_3/m(176)$	−0.928	0.000	1.00 BCl_3
32	SCl_2	$P2_12_12_1(19)$	−0.102	0.000	1.00 SCl_2
33	SCl	$Fdd2(43)$	−0.148	0.000	1.00 SCl
34	Cl_2O	$I4_1/amd(141)$	0.249	0.249	0.50 O_2 + 1.00 Cl_2
35	ClO_3	$Cc(9)$	0.133	0.133	1.50 O_2 + 0.50 Cl_2
36	Cl_2O_7	$C2/c(15)$	0.168	0.168	3.50 O_2 + 1.00 Cl_2
37	ClO_2	$Pbca(61)$	0.104	0.104	1.00 O_2 + 0.50 Cl_2
38	$LiAlB_{14}$	$C2(5)$	0.113	0.181	1.00 AlB_2 + 1.00 LiB_3 + 9.00 B
39	Li_5AlS_4	$P2_1/m(11)$	−1.339	0.000	1.00 Li_5AlS_4
40	Li_5AlO_4	$Pbca(61)$	−2.219	0.000	1.00 Li_5AlO_4
41	$LiAlO_2$	$R\bar{3}m(166)$	−2.761	0.000	1.00 $LiAlO_2$
42	$LiAl_5O_8$	$P4_332(212)$	−2.984	0.000	1.00 $LiAl_5O_8$
43	$LiAlCl_4$	$P2_1/c(14)$	−1.639	0.009	1.00 $AlCl_3$ + 1.00 LiCl
44	$Li_2B_2S_5$	$Cmcm(63)$	0.156	0.914	0.29 $Li_5B_7S_{13}$ + 0.29 Li_2S + 1.00 S
45	$Li_5B_7S_{13}$	$Cc(9)$	−0.791	0.000	1.00 $Li_5B_7S_{13}$

TABLE VIII. (*Continued.*)

No.	Material	Symmetry	Formation	Hull	Equilibrium
46	Li_3BS_3	$Pnma(62)$	−1.044	0.029	0.14 $Li_5B_7S_{13}$ + 1.14 Li_2S
47	$Li_2B_4O_7$	$I4_1cd(110)$	−2.445	0.002	0.50 $LiBO_2$ + 0.50 $Li_3B_7O_{12}$
48	$Li_3B_{11}O_{18}$	$P2_1/c(14)$	−2.427	0.011	1.00 $Li_3B_7O_{12}$ + 2.00 B_2O_3
49	LiB_3O_5	$Pna2_1(33)$	−2.435	0.007	0.33 $Li_3B_7O_{12}$ + 0.33 B_2O_3
50	Li_3BO_3	$P2_1/c(14)$	−2.262	0.000	1.00 Li_3BO_3
51	$Li_3B_7O_{12}$	$P\bar{1}(2)$	−2.449	0.000	1.00 $Li_3B_7O_{12}$
52	$Li_6B_4O_9$	$P2_1/c(14)$	−2.339	0.030	1.00 Li_3BO_3+ 3.00 $LiBO_2$
53	$LiBO_2$	$I\bar{4}2d(122)$	−2.432	0.000	1.00 $LiBO_2$
54	$LiClO_2$	$P4_2/ncm(138)$	−0.747	0.175	1.00 LiCl + 1.00 O_2
55	Li_5Cl_3O	$Fmm2(42)$	−1.617	0.226	1.00 Li_2O + 3.00 LiCl
56	$LiClO_4$	$Pnma(62)$	−0.613	0.002	1.00 LiCl + 2.00 O_2
57	Al_5BO_9	$Cmc2_1(36)$	−2.951	0.004	0.17 $Al_4B_6O_{15}$ + 2.17 Al_2O_3
58	$Al_4B_6O_{15}$	$R3(146)$	−2.680	0.000	1.00 $Al_4B_6O_{15}$
59	$AlSCl_7$	$Pc(7)$	−0.818	0.000	1.00 $AlSCl_7$
60	AlClO	$Pmmn(59)$	−2.389	0.0004	0.33 $AlCl_3$ + 0.33 Al_2O_3
61	Li_2AlBO_4	$P2_1/c(14)$	−2.549	0.048	1.00 $LiBO_2$ + 1.00 $LiAlO_2$
62	$Li_2AlB_5O_{10}$	$P2_1/c(14)$	−2.513	0.021	0.06 $Al_4B_6O_{15}$ + 0.67 $Li_3B_7O_{12}$ + 0.39 Al_2O_3
63	$LiAlB_2O_5$	$C2/c(15)$	−2.493	0.124	0.25 $LiBO_2$ + 0.25 $Li_3B_7O_{12}$ + 0.50 Al_2O_3
64	$Li_3AlB_2O_6$	$P\bar{1}(2)$	−2.490	0.052	2.00 $LiBO_2$ + 1.00 $LiAlO_2$
65	$Li_{7.5}B_{10}S_{18}Cl_{1.5}$	$C2/c(15)$	−0.840	0.000	1.00 $Li_{7.5}B_{10}S_{18}Cl_{1.5}$
66	$Li_5B_7O_{12.5}Cl$	$F23(196)$	−2.413	0.000	1.00 $Li_5B_7O_{12.5}Cl$
67	$Li_4B_7O_{12}Cl$	$R3c(161)$	−2.406	0.000	1.00 $Li_4B_7O_{12}Cl$
68	$Li_4B_7O_{12}Cl$	$F\bar{4}3c(219)$	−2.397	0.009	1.00 $Li_4B_7O_{12}Cl$
69	$Li_6B_7O_{13}Cl$	$R3c(161)$	−2.402	0.004	2.33 $LiBO_2$ + 0.66 $Li_5B_7O_{12.5}Cl$ + 0.33 LiCl
70	$Li_6B_7O_{13}Cl$	$Cc(9)$	−2.390	0.016	2.33 $LiBO_2$ + 0.66 $Li_5B_7O_{12.5}Cl$ + 0.33 LiCl
71	$Li_4Al_3B_4O_{12}Cl$	$R3c(161)$	−2.539	0.053	0.27 $LiBO_2$ + 0.60 $LiAl_5O_8$ + 0.54 $Li_5B_7O_{12.5}Cl$ + 0.47 LiCl
72	$Li_4Al_3B_4O_{12}Cl$	$F\bar{4}3c(219)$	−2.489	0.103	0.27 $LiBO_2$ + 0.60 $LiAl_5O_8$ + 0.54 $Li_5B_7O_{12.5}Cl$ + 0.47 LiCl
73	$Li_6Al_3B_4O_{13}Cl$	$R3c(161)$	−2.469	0.087	4.00 $LiBO_2$ + 0.50 $LiAl_5O_8$ + 0.50 $LiAlO_2$ + 1.00 LiCl
74	$Li_6Al_3B_4O_{13}Cl$	$Cc(9)$	−2.476	0.080	4.00 $LiBO_2$ + 0.50 $LiAl_5O_8$ + 0.50 $LiAlO_2$ + 1.00 LiCl
75	$Li_4B_7S_{12}Cl$	$R3c(161)$	−0.754	0.015	0.50 $Li_{7.5}B_{10}S_{18}Cl_{1.5}$ + 1.00 BS_2 + 1.00 BS + 0.25 LiCl
76	$Li_4B_7S_{12}Cl$	$F\bar{4}3c(219)$	−0.757	0.013	0.50 $Li_{7.5}B_{10}S_{18}Cl_{1.5}$ + 1.00 BS_2 + 1.00 BS + 0.25 LiCl
77	$Li_6B_7S_{13}Cl$	$R3c(161)$	−0.858	0.011	1.00 $Li_5B_7S_{13}$ + 1.00 LiCl
78	$Li_6B_7S_{13}Cl$	$Cc(9)$	−0.861	0.008	1.00 $Li_5B_7S_{13}$ + 1.00 LiCl
79	$Li_4Al_3B_4S_{12}Cl$	$R3c(161)$	−0.928	0.059	0.57 $Li_5B_7S_{13}$ + 0.03 Li_5AlS_4 + 1.49 Al_2S_3 + 1.00 LiCl
80	$Li_4Al_3B_4S_{12}Cl$	$F\bar{4}3c(219)$	−0.893	0.095	0.57 $Li_5B_7S_{13}$ + 0.03 Li_5AlS_4 + 1.49 Al_2S_3 + 1.00 LiCl
81	$Li_6Al_3B_4S_{13}Cl$	$R3c(161)$	−0.990	0.045	0.57 $Li_5B_7S_{13}$ + 0.43 Li_5AlS_4 + 1.29 Al_2S_3 + 1.00 LiCl
82	$Li_6Al_3B_4S_{13}Cl$	$Cc(9)$	−1.001	0.034	0.57 $Li_5B_7S_{13}$ + 0.43 Li_5AlS_4 + 1.29 Al_2S_3 + 1.00 LiCl

TABLE IX. Decomposition equations and corresponding reaction energies at critical applied voltages or chemical potentials. Results are listed in eight subtables for the each of the Li (thio)boracites in this study based on their most stable structural form. In each subtable, the first column gives the fixed value of $\phi = -\mu_{Li}(\phi)/e$ in units of Volts. The second column presents the computed values of $\overline{\Delta\Omega}$ in units of eV/atom, defined by Eq. (22) and derived from Eq. (21) corresponding to the most energetically favorable reaction, which is listed in the final column. That reaction is found using the Pymatgen software [39] according to the lowest energy of $\Delta\Omega$(system, ϕ, Δn_{Li}) found for the given electrolyte (R) and voltage (ϕ) according to Eq. (20). It should be noted that the stoichiometric coefficients presented each reaction equation have been rounded to three decimal places. As explained in Sec. IV, the formation energies of elemental Li, Al, B, or S and molecular dimers $\frac{1}{2}$ O_2 or $\frac{1}{2}$ Cl_2 are each zero.

(a) $Li_4B_7O_{12}Cl$

ϕ (V)	$\overline{\Delta\Omega}$ (eV/atom)	Reaction onset
0.000	−0.714	$Li_4B_7O_{12}Cl$ + 23.333 Li → 12 Li_2O + 2.333 LiB_3 + LiCl
0.311	−0.351	$Li_4B_7O_{12}Cl$ + 10 Li → 4 Li_3BO_3 + LiB_3 + LiCl
0.661	−0.176	$Li_4B_7O_{12}Cl$ + 8.471 Li → 3.824 Li_3BO_3 + 0.529 B_6O + LiCl
0.860	−0.092	$Li_4B_7O_{12}Cl$ + 2.909 Li → 5.909 $LiBO_2$ + 0.182 B_6O + LiCl
1.491	0.000	$Li_4B_7O_{12}Cl$ → $Li_4B_7O_{12}Cl$
3.860	0.000	$Li_4B_7O_{12}Cl$ → $Li_3B_7O_{12}$ + 0.5 Cl_2 + Li
3.881	−0.001	$Li_4B_7O_{12}Cl$ → 3.5 B_2O_3 + 0.75 O_2 + 0.5 Cl_2 + 4 Li
5.000	−0.225	$Li_4B_7O_{12}Cl$ → 3.5 B_2O_3 + 0.75 O_2 + 0.5 Cl_2 + 4 Li

TABLE IX. (*Continued.*)

(b) $Li_6B_7O_{13}Cl$

ϕ (V) (eV)	$\overline{\Delta\Omega}$ (eV/atom)	Reaction onset
0.000	−0.600	$Li_6B_7O_{13}Cl + 23.33\ Li \rightarrow 13\ Li_2O + 2.333\ LiB_3 + LiCl$
0.311	−0.254	$Li_6B_7O_{13}Cl + 8.889\ Li \rightarrow 4.333\ Li_3BO_3 + 0.889\ LiB_3 + LiCl$
0.661	−0.106	$Li_6B_7O_{13}Cl + 7.529\ Li \rightarrow 4.176\ Li_3BO_3 + 0.471\ B_6O + LiCl$
0.860	−0.034	$Li_6B_7O_{13}Cl + 1.455\ Li \rightarrow 6.455\ LiBO_2 + 0.091\ B_6O + LiCl$
1.357	0.000	$Li_6B_7O_{13}Cl \rightarrow Li_6B_7O_{13}Cl$
3.607	0.000	$Li_6B_7O_{13}Cl \rightarrow Li_4B_7O_{12}Cl + 0.5\ O_2 + 2\ Li$
3.860	−0.024	$Li_6B_7O_{13}Cl \rightarrow Li_3B_7O_{12} + 0.5\ O_2 + 0.5\ Cl_2 + 3\ Li$
3.881	−0.027	$Li_6B_7O_{13}Cl \rightarrow 3.5\ B_2O_3 + 1.25\ O_2 + 0.5\ Cl_2 + 6\ Li$
5.000	−0.347	$Li_6B_7O_{13}Cl \rightarrow 3.5\ B_2O_3 + 1.25\ O_2 + 0.5\ Cl_2 + 6\ Li$

(c) $Li_4Al_3B_4O_{12}Cl$

ϕ (V)	$\overline{\Delta\Omega}$ (eV/atom)	Reaction onset
0.000	−0.520	$Li_4Al_3B_4O_{12}Cl + 28.33\ Li \rightarrow 3\ Li_2Al + 12\ Li_2O + 1.333\ LiB_3 + LiCl$
0.079	−0.408	$Li_4Al_3B_4O_{12}Cl + 13.33\ Li \rightarrow 3\ Li_5AlO_4 + 1.333\ LiB_3 + LiCl$
0.353	−0.225	$Li_4Al_3B_4O_{12}Cl + 6.667\ Li \rightarrow 2\ Li_3BO_3 + 3\ LiAlO_2 + 0.667\ LiB_3 + LiCl$
0.661	−0.122	$Li_4Al_3B_4O_{12}Cl + 5.647\ Li \rightarrow 1.882\ Li_3BO_3 + 0.353\ B_6O + 3\ LiAlO_2 + LiCl$
0.860	−0.066	$Li_4Al_3B_4O_{12}Cl + 2.909\ Li \rightarrow 2.909\ LiBO_2 + 0.182\ B_6O + 3\ LiAlO_2 + LiCl$
1.284	−0.004	$Li_4Al_3B_4O_{12}Cl + 1.164\ Li \rightarrow 3.564\ LiBO_2 + 0.073\ B_6O + 0.6\ LiAl_5O_8 + LiCl$
1.358	0.000	$Li_4Al_3B_4O_{12}Cl \rightarrow Li_4Al_3B_4O_{12}Cl$
3.629	0.000	$Li_4Al_3B_4O_{12}Cl \rightarrow 0.571\ Li_4B_7O_{12}Cl + 0.429\ LiCl + 0.321\ O_2 + 1.5\ Al_2O_3 + 1.286\ Li$
3.687	−0.004	$Li_4Al_3B_4O_{12}Cl \rightarrow 0.571\ Li_4B_7O_{12}Cl + 0.321\ O_2 + 1.5\ Al_2O_3 + 0.214\ Cl_2 + 1.714\ Li$
3.821	−0.015	$Li_4Al_3B_4O_{12}Cl \rightarrow 0.667\ Al_4(B_2O_5)_3 + 0.75\ O_2 + 0.167\ Al_2O_3 + 0.5\ Cl_2 + 4\ Li$
5.000	−0.251	$Li_4Al_3B_4O_{12}Cl \rightarrow 0.667\ Al_4(B_2O_5)_3 + 0.75\ O_2 + 0.167\ Al_2O_3 + 0.5\ Cl_2 + 4\ Li$

(d) $Li_6Al_3B_4O_{13}Cl$

ϕ (V)	$\overline{\Delta\Omega}$ (eV/atom)	Reaction onset
0.000	−0.434	$Li_6Al_3B_4O_{13}Cl + 28.330\ Li \rightarrow 3\ Li_2Al + 13\ Li_2O + 1.333\ LiB_3 + LiCl$
0.079	−0.328	$Li_6Al_3B_4O_{13}Cl + 13.330\ Li \rightarrow 3\ Li_5AlO_4 + Li_2O + 1.333\ LiB_3 + LiCl$
0.311	−0.180	$Li_6Al_3B_4O_{13}Cl + 12.220\ Li \rightarrow 3\ Li_5AlO_4 + 0.333\ Li_3BO_3 + 1.222\ LiB_3 + LiCl$
0.353	−0.155	$Li_6Al_3B_4O_{13}Cl + 5.556\ Li \rightarrow 2.333\ Li_3BO_3 + 3\ LiAlO_2 + 0.556\ LiB_3 + LiCl$
0.661	−0.074	$Li_6Al_3B_4O_{13}Cl + 4.706\ Li \rightarrow 2.235\ Li_3BO_3 + 0.294\ B_6O + 3\ LiAlO_2 + LiCl$
0.860	−0.029	$Li_6Al_3B_4O_{13}Cl + 1.455\ Li \rightarrow 3.455\ LiBO_2 + 0.091\ B_6O + 3\ LiAlO_2 + LiCl$
1.284	0.000	$Li_6Al_3B_4O_{13}Cl \rightarrow Li_6Al_3B_4O_{13}Cl$
3.360	0.000	$Li_6Al_3B_4O_{13}Cl \rightarrow 4\ LiBO_2 + 0.600\ LiAl_5O_8 + LiCl + 0.100\ O_2 + 0.400\ Li$
3.507	−0.003	$Li_6Al_3B_4O_{13}Cl \rightarrow 4\ LiBO_2 + LiCl + 0.250\ O_2 + 1.5\ Al_2O_3 + Li$
3.687	−0.031	$Li_6Al3B_4O_{13}Cl \rightarrow 0.571\ Li_4B7O12Cl + 0.821\ O_2 + 1.500\ Al_2O_3 + 0.214\ Cl_2 + 3.714\ Li$
3.821	−0.054	$Li_6Al3B_4O_{13}Cl \rightarrow 0.667\ Al_4(B_2O_5$
5.000	−0.391	$Li_6Al3B_4O_{13}Cl \rightarrow 0.667\ Al_4(B_2O_5$

(e) $Li_4B_7S_{12}Cl$

ϕ (V)	$\overline{\Delta\Omega}$ (eV/atom)	Reaction onset
0.000	−1.821	$Li_4B_7S_{12}Cl + 23.33\ Li \rightarrow 2.333\ LiB_3 + 12\ Li_2S + LiCl$
0.866	−0.811	$Li_4B_7S_{12}Cl + 21\ Li \rightarrow 12\ Li_2S + LiCl + 7\ B$
1.595	−0.045	$Li_4B_7S_{12}Cl + 1.615\ Li \rightarrow 0.923\ Li_5B_7S_{13} + LiCl + 0.539\ B$
1.606	−0.044	$Li_4B_7S_{12}Cl + 1.167\ Li \rightarrow 0.833\ Li_5B_7S_{13} + 1.167\ BS + LiCl$
2.360	0.000	$Li_4B_7S_{12}Cl \rightarrow Li_4B_7S_{12}Cl$
2.491	0.000	$Li_4B_7S_{12}Cl \rightarrow 5\ BS_2 + 2\ BS + LiCl + 3\ Li$
2.686	−0.029	$Li_4B_7S_{12}Cl \rightarrow 5.333\ BS_2 + 1.333\ BS + 0.333\ BCl_3 + 4\ Li$
5.000	−0.492	$Li_4B_7S_{12}Cl \rightarrow 5.333\ BS_2 + 1.333\ BS + 0.333\ BCl_3 + 4\ Li$

(f) $Li_6B_7S_{13}Cl$

ϕ (V)	$\overline{\Delta\Omega}$ (eV/atom)	Reaction onset
0.000	−1.692	$Li_6B_7S_{13}Cl + 23.33\ Li \rightarrow 2.333\ LiB_3 + 13\ Li_2S + LiCl$
0.866	−0.730	$Li_6B_7S_{13}Cl + 21\ Li \rightarrow 13\ Li_2S + LiCl + 7\ B$
1.595	0.000	$Li_6B_7S_{13}Cl \rightarrow Li_6B_7S_{13}Cl$
2.454	0.000	$Li_6B_7S_{13}Cl \rightarrow 6\ BS_2 + BS + LiCl + 5\ Li$
2.686	−0.055	$Li_6B_7S_{13}Cl \rightarrow 6.333\ BS_2 + 0.333\ BS + 0.333\ BCl_3 + 6\ Li$
5.000	−0.716	$Li_6B_7S_{13}Cl \rightarrow 6.333\ BS_2 + 0.333\ BS + 0.333\ BCl_3 + 6\ Li$

TABLE IX. (*Continued.*)

(g) $Li_4Al_3B_4S_{12}Cl$		
ϕ (V)	$\overline{\Delta\Omega}$ (eV/atom)	Reaction onset
0.000	−1.588	$Li_4Al_3B_4S_{12}Cl + 28.33\ Li \rightarrow 3\ Li_2Al + 1.333\ LiB_3 + 12\ Li_2S + LiCl$
0.126	−1.409	$Li_4Al_3B_4S_{12}Cl + 25.33\ Li \rightarrow 3\ LiAl + 1.333\ LiB_3 + 12\ Li_2S + LiCl$
0.351	−1.124	$Li_4Al_3B_4S_{12}Cl + 23.33\ Li \rightarrow\ LiAl_3 + 1.333\ LiB_3 + 12\ Li_2S + LiCl$
0.354	−1.121	$Li_4Al_3B_4S_{12}Cl + 22.33\ Li \rightarrow 1.333\ LiB_3 + 12\ Li_2S + LiCl + 3\ Al$
0.542	−0.911	$Li_4Al_3B_4S_{12}Cl + 21\ Li \rightarrow 2\ AlB_2 + 12\ Li_2S + LiCl + Al$
1.003	−0.427	$Li_4Al_3B_4S_{12}Cl + 18\ Li \rightarrow\ Li_5AlS_4 + 2\ AlB_2 + 8\ Li_2S + LiCl$
1.075	−0.362	$Li_4Al_3B_4S_{12}Cl + 12\ Li \rightarrow 3\ Li_5AlS_4 + LiCl + 4\ B$
1.664	−0.008	$Li_4Al_3B_4S_{12}Cl + 4\ Li \rightarrow 1.400\ Li_5AlS_4 + 4\ BS + 0.800\ Al_2S_3 + LiCl$
1.706	0.000	$Li_4Al_3B_4S_{12}Cl \rightarrow\ Li_4Al_3B_4S_{12}Cl$
2.122	0.000	$Li_4Al_3B_4S_{12}Cl \rightarrow 0.571\ Li_5B7S_{13} + 1.5\ Al_2S_3 + LiCl + 0.071\ S + 0.143\ Li$
2.415	−0.002	$Li_4Al_3B_4S_{12}Cl \rightarrow 0.5\ Li_5B7S_{13} + 0.5\ BS_2 + 1.5\ Al_2S_3 + LiCl + 0.5\ Li$
2.454	−0.003	$Li_4Al_3B_4S_{12}Cl \rightarrow 3.5\ BS_2 + 0.5\ BS + 1.5\ Al_2$
2.457	−0.004	$Li_4Al_3B_4S_{12}Cl \rightarrow 4\ BS_2 + 1.333\ Al_2S_3 + 0.333\ AlCl_3 + 4\ Li$
5.000	−0.512	$Li_4Al_3B_4S_{12}Cl \rightarrow 4\ BS_2 + 1.333\ Al_2S_3 + 0.333\ AlCl_3 + 4\ Li$
(h) $Li_6Al_3B_4S_{13}Cl$		
ϕ (V)	$\overline{\Delta\Omega}$ (eV/atom)	Reaction onset
0.000	−1.506	$Li_6Al_3B_4S_{13}Cl + 28.33\ Li \rightarrow 3\ Li_2Al + 1.333\ LiB_3 + 13\ Li_2S + LiCl$
0.126	−1.336	$Li_6Al_3B_4S_{13}Cl + 25.33\ Li \rightarrow 3\ LiAl + 1.333\ LiB_3 + 13\ Li_2S + LiCl$
0.351	−1.065	$Li_6Al_3B_4S_{13}Cl + 23.33\ Li \rightarrow\ LiAl_3 + 1.333\ LiB_3 + 13\ Li_2S + LiCl$
0.354	−1.061	$Li_6Al_3B_4S_{13}Cl + 22.33\ Li \rightarrow 1.333\ LiB_3 + 13\ Li_2S + LiCl + 3\ Al$
0.542	−0.862	$Li_6Al_3B_4S_{13}Cl + 21\ Li \rightarrow 2\ AlB_2 + 13\ Li_2S + LiCl + Al$
1.003	−0.400	$Li_6Al_3B_4S_{13}Cl + 18\ Li \rightarrow\ Li_5AlS_4 + 2\ AlB_2 + 9\ Li_2S + LiCl$
1.075	−0.339	$Li_6Al_3B_4S_{13}Cl + 12\ Li \rightarrow 3\ Li_5AlS_4 + Li_2S + LiCl + 4\ B$
1.595	−0.041	$Li_6Al_3B_4S_{13}Cl + 10.38\ Li \rightarrow 0.077\ Li_5B7S_{13} + 3\ Li_5AlS_4 + LiCl + 3.462\ B$
1.606	−0.036	$Li_6Al_3B_4S_{13}Cl + 10\ Li \rightarrow 3\ Li_5AlS_4 + BS + LiCl + 3\ B$
1.664	−0.008	$Li_6Al_3B_4S_{13}Cl + 4\ Li \rightarrow 1.8\ Li_5AlS_4 + 4\ BS + 0.6\ Al_2S_3 + LiCl$
1.706	0.000	$Li_6Al_3B_4S_{13}Cl \rightarrow\ Li_6Al_3B_4S_{13}Cl$
2.117	0.000	$Li_6Al_3B_4S_{13}Cl \rightarrow 0.571\ Li_5B7S_{13} + 1.5\ Al_2S_3 + LiCl + 1.071\ S + 2.143\ Li$
2.415	−0.031	$Li_6Al_3B_4S_{13}Cl \rightarrow 4\ BS_2 + 1.5\ Al_2S_3 + LiCl + 0.5\ S + 5\ Li$
2.555	−0.064	$Li_6Al_3B_4S_{13}Cl \rightarrow 4\ BS_2 + 1.333\ Al_2S_3 + 0.333\ AlCl_3 + S + 6\ Li$
5.000	−0.762	$Li_6Al_3B_4S_{13}Cl \rightarrow 4\ BS_2 + 1.333\ Al_2S_3 + 0.333\ AlCl_3 + S + 6\ Li$

TABLE X. Equilibrium phases and changes in the grand canonical potential $\Delta\Omega$ for Li (thio)boracite electrolytes in an idealized battery configuration. The anode μ_{Li} is set to the chemical potential of bulk lithium, μ^0_{Li}, while the cathode μ_{Li} is adjusted to $\mu^0_{Li} - 5$ eV to simulate a high voltage of 5 V. The $\overline{\Delta\Omega}$ energies are reported in units of eV/atom.

Materials	Phases at $\phi = 0$ V	$\overline{\Delta\Omega}(\phi = 0\ V)$	Phases atr $\phi = 5$ V	$\overline{\Delta\Omega}(\phi = 5\ V)$
$Li_4B_7O_{12}Cl$	Li_2O, LiB_3, $LiCl$	−0.714	B_2O_3, O_2, Cl_2	−0.225
$Li_6B_7O_{13}Cl$	Li_2O, LiB_3, $LiCl$	−0.600	B_2O_3, O_2, Cl_2	−0.347
$Li_4Al_3B_4O_{12}Cl$	Li_2Al, Li_2O, LiB_3, $LiCl$	−0.519	$Al_4B_6O_{15}$, O_2, Al_2O_3, Cl_2	−0.251
$Li_6Al_3B_4O_{13}Cl$	Li_2Al, Li_2O, LiB_3, $LiCl$	−0.434	$Al_4B_6O_{15}$, O_2, Al_2O_3, Cl_2	−0.391
$Li_4B_7S_{12}Cl$	LiB_3, Li_2S, $LiCl$	−1.821	BS_2, BS, BCl_3	−0.492
$Li_6B_7S_{13}Cl$	LiB_3, Li_2S, $LiCl$	−1.692	BS_2, BS, BCl_3	−0.716
$Li_4Al_3B_4S_{12}Cl$	Li_2Al, LiB_3, Li_2S, $LiCl$	−1.588	BS_2, Al_2S_3, $AlCl_3$	−0.512
$Li_6Al_3B_4S_{13}Cl$	Li_2Al, LiB_3, Li_2S, $LiCl$	−1.506	BS_2, Al_2S_3, $AlCl_3$, S	−0.762

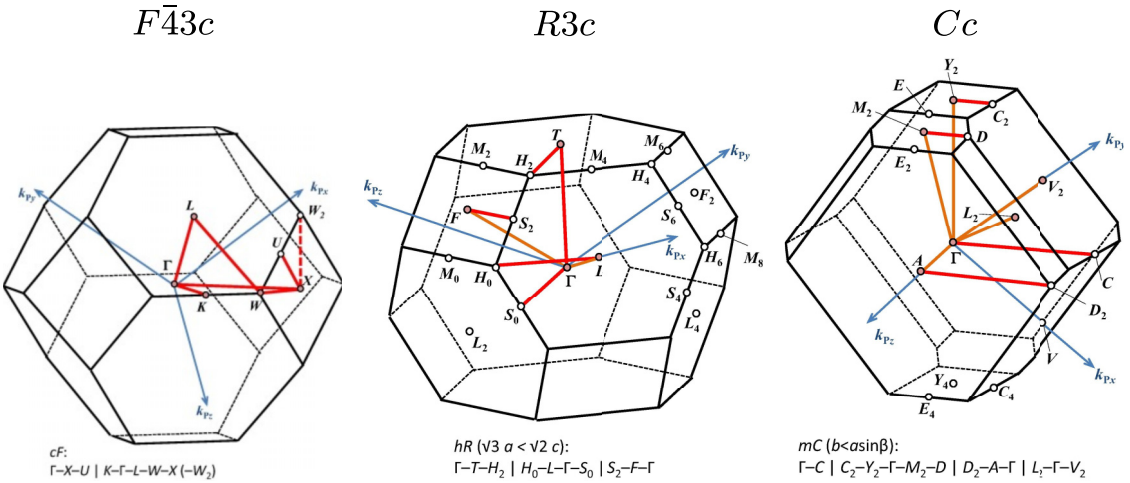

FIG. 19. Brillouin zone diagrams from Ref. [60] reproduced with permission from the publisher.

[1] W. Jeitschko, T. A. Bither, and P. E. Bierstedt, Acta Crystallogr. Sect. B **33**, 2767 (1977), detailed crystal parameters associated with this paper are available as cif files from various crystallography databases.

[2] D. Tan, F. Wang, T. Pietsch, M. A. Grasser, T. Doert, and M. Ruck, ACS Appl. Energy Mater. **2**, 5140 (2019).

[3] Y. Li and N. A. W. Holzwarth, Phys. Rev. Mater. **6**, 025401 (2022).

[4] K. Kajihara, N. Tezuka, M. Shoji, J. Wakasugi, H. Munakata, and K. Kanamura, Bull. Chem. Soc. Jpn. **90**, 1279 (2017).

[5] T. Katsumata, Y. Aoki, K. Fushimi, K. Otsuka, K. Ueda, and Y. Inaguma, Solid State Ionics **380**, 115921 (2022).

[6] K. Kaup, K. Bishop, A. Assoud, J. Liu, and L. F. Nazar, J. Am. Chem. Soc. **143**, 6952 (2021).

[7] Information Systems and Wake Forest University, WFU High Performance Computing Facility (2021).

[8] P. Hohenberg and W. Kohn, Phys. Rev. **136**, B864 (1964).

[9] W. Kohn and L. J. Sham, Phys. Rev. **140**, A1133 (1965).

[10] P. Giannozzi, S. de Gironcoli, P. Pavone, and S. Baroni, Phys. Rev. B **43**, 7231 (1991).

[11] X. Gonze, Phys. Rev. B **55**, 10337 (1997).

[12] X. Gonze and C. Lee, Phys. Rev. B **55**, 10355 (1997).

[13] S. Baroni, S. De Gironcoli, A. Dal Corso, and P. Giannozzi, Rev. Mod. Phys. **73**, 515 (2001).

[14] P. Giannozzi and S. Baroni, in *Handbook of Materials Modeling*, edited by S. Yip (Springer, New York, 2005), pp. 195–214.

[15] P. E. Blöchl, Phys. Rev. B **50**, 17953 (1994).

[16] J. P. Perdew, A. Ruzsinszky, G. I. Csonka, O. A. Vydrov, G. E. Scuseria, L. A. Constantin, X. Zhou, and K. Burke, Phys. Rev. Lett. **100**, 136406 (2008).

[17] N. A. W. Holzwarth, A. R. Tackett, and G. E. Matthews, Comput. Phys. Commun. **135**, 329 (2001).

[18] X. Gonze, F. Jollet, F. A. Araujo, D. Adams, B. Amadon, T. Applencourt, C. Audouze, J.-M. Beuken, J. Bieder, A. Bokhanchuk *et al.*, Comput. Phys. Commun. **205**, 106 (2016).

[19] X. Gonze, B. Amadon, G. Antonius, F. Arnardi, L. Baguet, J.-M. Beuken, J. Bieder, F. Bottin, J. Bouchet, E. Bousquet *et al.*, Comput. Phys. Commun. **248**, 107042 (2020).

[20] P. Giannozzi, O. Andreussi, T. Brumme, O. Bunau, M. Buongiorno Nardelli, M. Calandra, R. Car, C. Cavazzoni, D. Ceresoli, M. Cococcioni *et al.*, J. Phys.: Condens. Matter **29**, 465901 (2017).

[21] P. Giannozzi, O. Baseggio, P. Bonfà, D. Brunato, R. Car, I. Carnimeo, C. Cavazzoni, S. de Gironcoli, P. Delugas, F. Ferrari Ruffino *et al.*, J. Chem. Phys. **152**, 154105 (2020).

[22] Y. Li, Z. D. Hood, and N. A. W. Holzwarth, Phys. Rev. Mater. **4**, 045406 (2020).

[23] M. Born and K. Huang, *Dynamical Theory of Crystal Lattices* (Oxford University Press, Oxford, 1954); Appendix VIII expands the ideas presented by M. Born and R. Oppenheimer, Ann. d. Phys. **54**, 457 (1927).

[24] A. Jain, S. P. Ong, G. Hautier, W. Chen, W. D. Richards, S. Dacek, S. Cholia, D. Gunter, D. Skinner, G. Ceder, and K. A. Persson, APL Mater. **1**, 011002 (2013).

[25] J. E. Saal, S. Kirklin, M. Aykol, B. Meredig, and C. Wolverton, JOM **65**, 1501 (2013).

[26] S. Kirklin, J. E. Saal, B. Meredig, A. Thompson, J. W. Doak, M. Aykol, S. Rühl, and C. Wolverton, npj Comput. Mater. **1**, 15010 (2015).

[27] H. T. Stokes and D. M. Hatch, J. Appl. Cryst. **38**, 237 (2005).

[28] K. Momma and F. Izumi, Appl Crystallogr. **44**, 1272 (2011), Code available from the website http://jp-minerals.org/vesta/en/.

[29] XMGRACE software available at the website, https://plasma-gate.weizmann.ac.il/pub/grace (2008).

[30] M. I. Aroyo, J. M. Perez-Mato, D. Orobengoa, E. Tasci, G. De La Flor, and A. Kirov, Bulg. Chem. Commun. **43**, 183 (2011), Also note that this space group information is also available from the International Union of Crystallography, which hosts the website for the International Tables for Crystallography, https://doi.org/10.1107/97809553602060000001.

[31] A. Levasseur, C. Fouassier, and P. Hagenmuller, Mater. Res. Bull. **6**, 15 (1971).

[32] A. Levasseur and D. J. Lloyd, J. Solid State Chem. **8**, 318 (1973).

[33] J.-M. Réau, A. Levasseur, G. Magniez, and B. Calès, Mater. Res. Bull. **11**, 1087 (1976).

[34] B. Calès, A. Levasseur, C. Fouassier, J. M. Réau, and P. Hagenmuller, Solid State Commun. **24**, 323 (1977).

[35] W. Jeitschko and T. A. Bither, Zeitschrift für Naturforschung B **27**, 1423 (1972).

[36] See Supplemental Material at http://link.aps.org/supplemental/10.1103/PhysRevMaterials.8.065401 for Part I (SI1.pdf) includes detailed structural information, electronic partial density of states, and phonon band dispersions and density of states of the Li (thio)boracite materials. Additional Ref. [66] is cited. Part II (SI2.pdf) includes detailed structural information about ground-state structures of the related materials listed in Appendix B and Table VIII of the paper.

[37] S. P. Ong, L. Wang, B. Kang, and G. Ceder, Chem. Mater. **20**, 1798 (2008).

[38] M. Hellenbrandt, Crystallogra. Rev. **10**, 17 (2004).

[39] S. P. Ong, W. D. Richards, A. Jain, G. Hautier, M. Kocher, S. Cholia, D. Gunter, V. L. Chevrier, K. A. Persson, and G. Ceder, Comput. Mater. Sci. **68**, 314 (2013).

[40] W. Sun, S. T. Dacek, S. P. Ong, G. Hautier, A. Jain, W. D. Richards, A. C. Gamst, K. A. Persson, and G. Ceder, Sci. Adv. **2**, e1600225 (2016).

[41] M. Vlasse, A. Levasseur, and P. Hagenmuller, Solid State Ionics **2**, 33 (1981).

[42] N. Tezuka, Y. Okawa, K. Kajihara, and K. Kanamura, J. Ceram. Soc. Jpn. **125**, 348 (2017).

[43] Y. Zhu, X. He, and Y. Mo, ACS Appl. Mater. Interfaces **7**, 23685 (2015).

[44] W. D. Richards, L. J. Miara, Y. Wang, J. C. Kim, and G. Ceder, Chem. Mater. **28**, 266 (2016).

[45] Y. Zhu, X. He, and Y. Mo, J. Mater. Chem. A **4**, 3253 (2016).

[46] K. T. Butler, G. Sai Gautam, and P. Canepa, npj Comput. Mater. **5**, 19 (2019).

[47] T. Chen, G. Ceder, G. Sai Gautam, and P. Canepa, Front. Chem. **7**, 24 (2019).

[48] Y. Xiao, Y. Wang, S.-H. Bo, J. C. Kim, L. J. Miara, and G. Ceder, Nat. Rev. Mater. **5**, 105 (2020).

[49] M. K. Aydinol, A. F. Kohan, G. Ceder, K. Cho, and J. Joannopoulos, Phys. Rev. B **56**, 1354 (1997).

[50] S. P. Ong, O. Andreussi, Y. Wu, N. Marzari, and G. Ceder, Chem. Mater. **23**, 2979 (2011).

[51] M. V. Reddy, C. M. Julien, A. Mauger, and K. Zaghib, Nanomaterials **10**, 1606 (2020).

[52] Y. Okuno, J. Haruyama, and Y. Tateyama, ACS Appl. Energy Mater. **3**, 11061 (2020).

[53] Y. Tian, T. Shi, W. D. Richards, J. Li, J. C. Kim, S.-H. Bo, and G. Ceder, Energy Environ. Sci. **10**, 1150 (2017).

[54] D.-H. Wang, H.-Y. Zhou, C.-H. Hu, Y. Zhong, A. R. Oganov, and G.-H. Rao, Phys. Chem. Chem. Phys. **19**, 8471 (2017).

[55] A. A. Maradudin, E. W. Montroll, G. H. Weiss, and I. P. Ipatova, *Theory of Lattice Dynamics in the Harmonic Approximation*, 2nd ed., Solid state physics: Supplement (Academic Press, New York, 1971), Vol. 3.

[56] K. Parlinski, Z. Q. Li, and Y. Kawazoe, Phys. Rev. Lett. **78**, 4063 (1997).

[57] A. Togo, L. Chaput, T. Tadano, and I. Tanaka, J. Phys.: Condens. Matter **35**, 353001 (2023).

[58] A. Togo, J. Phys. Soc. Jpn. **92**, 012001 (2023).

[59] Y. Li, W. C. Kerr, and N. A. W. Holzwarth, J. Phys.: Condens. Matter **32**, 055402 (2020).

[60] Y. Hinuma, G. Pizzi, Y. Kumagai, F. Oba, and I. Tanaka, Comput. Mater. Sci. **128**, 140 (2017), online tool available from the website, https://www.materialscloud.org/work/tools/seekpath.

[61] In order to check the numerical accuracy of the imaginary modes in $R3c$ $Li_6B_7S_{13}Cl$, we repeated the calculations checking the convergence parameters and also using density functional perturbation theory methodology with both ABINIT and QUANTUM ESPRESSO. Essentially the same results were obtained in all of the tests.

[62] G. Petretto, S. Dwaraknath, H. P.C. Miranda, D. Winston, M. Giantomassi, M. J. van Setten, X. Gonze, K. A. Persson, G. Hautier, and G.-M. Rignanese, Scientific Data **5**, 180065 (2018).

[63] K. Kaup, A. Assoud, J. Liu, and L. F. Nazar, Angew. Chem. Int. Ed. **60**, 6975 (2021).

[64] Y. Li and N. A. W. Holzwarth, Phys. Rev. Mater. **6**, 045403 (2022).

[65] W. Setyawan and S. Curtarolo, Comput. Mater. Sci. **49**, 299 (2010).

[66] L. E. Rush, Z. D. Hood, and N. A. W. Holzwarth, Phys. Rev. Mater. **1**, 075405 (2017).